Unveiling and understanding the remarkable enhancement in the catalytic activity by the defect creation in UIO-66 during the catalytic transfer hydrodeoxygenation of vanillin with isopropanol

Ashish Kumar Kar [a,1], Ranjini Sarkar [b,c], Arjun K. Manal [a], Ravi Kumar [c], Sudip Chakraborty [b,*], Rajeev Ahuja [d,e], Rajendra Srivastava [a,*,2]

[a] *Catalysis Research Laboratory, Department of Chemistry, Indian Institute of Technology, Ropar, Rupnagar 140001, India*
[b] *Materials Theory for Energy Scavenging (MATES) Lab, Harish-Chandra Research Institute (HRI) Allahabad, HBNI, Chhatnag Road, Jhunsi, Prayagraj (Allahabad) 211019 India*
[c] *Ceramic Technologies Group-Center of Excellence in Materials and Manufacturing for Futuristic Mobility, Indian Institute of Technology-Madras (IIT Madras), Chennai, 600036, India*
[d] *Department of Physics, Indian Institute of Technology Ropar, Rupnagar, Punjab 140001, India*
[e] *Condensed Matter Theory Group, Department of Physics and Astronomy, Uppsala University, Uppsala SE 75120, Sweden*

ARTICLE INFO

ABSTRACT

The catalytic transfer hydrodeoxygenation of vanillin is generally achieved using noble metal-based catalysts. Herein, we report a mechanistic investigation of the catalytic transfer hydrodeoxygenation (CTHDO) of vanillin over a defect-induced UIO-66 MOF. The remarkable enhancement in the CTHDO of vanillin was due to the unique structural features of the defect-induced UIO-66 MOF. The defect creation was confirmed using PXRD, N_2-sorption, FT-IR, XPS, HRTEM, dissolution ^1H NMR, and quantified by TGA. The linker deficiency created Lewis acid and dynamic Bronsted acid and was confirmed by the NH_3-TPD and CD_3CN drift FT-IR. The periodic density functional theory calculations were conducted to elucidate the reaction pathway and mechanism. Density function theory, poisoning studies, control reactions, and quantified defect sites elucidate the active sites of the UIO-66$_{def}$ involved in the CTHDO of vanillin with isopropanol. The catalyst was efficiently recycled and retained its activity and structural features after multiple recycles.

1. Introduction

The sustainable valorization of biomass-derived lignin model oil to liquid fuels should be established to embark on future energy demands by considering its renewability. The complex structure of organic compounds bearing carbonyl, phenolic, and alkoxy groups derived from lignin model oil, requires catalytic valorization to produce liquid fuels [1–4]. Furfural, HMF, levulinic acid, aromatic ethers, etc., are popular lignocellulosic biomass model compounds employed as feedstocks for producing valuable chemicals and fuels [5–7]. Vanillin is a significant component of lignin model oil. The vanillin conversion to 2-methoxy-methyl phenol (MMP) is an essential transformation because MMP can fulfil future chemicals and fuel requirements. MMP is not only a potential biofuel, but it is also used as a precursor in fragrances and drugs

showing antibacterial and anti-insecticidal properties. It is also used to manufacture food flavouring compounds and feedstock for resin synthesis [8,9]. The catalytic processes, including hydrogenation, hydrodeoxygenation, hydrogenolysis, etc., have been adopted to valorize vanillin and other lignin-derived compounds [10–12]. These catalytic processes are employed to minimize the oxygen content in the bio-oil to make them thermally stable and convenient for their fuel applications [13]. The efficient adsorption and activation of H_2 require higher temperature and H_2 pressure (on several catalysts) and dedicated reaction setups to conduct the above-mentioned catalytic processes. Moreover, it is difficult to control the H_2 stoichiometry during the reduction catalysis, which eventually leads to over-reduction with a loss of specific product selectivity. Transfer hydrogenation is a sustainable strategy for these reactions without employing highly pressurized H_2 gas [14,15]. In the

---

transfer hydrogenation process, the hydrogen atom of the donor molecules, known as a hydrogen carrier, transfers the H-atom to the target molecules. Various representative H_2 carriers like formic acid, hydrazine hydrate, isopropanol (IPA), etc., have been employed [16–20]. Among these H_2 carriers, IPA is an abundant, inexpensive, non-toxic, non-corrosive, and holds the unique feature of acting as solvent itself, hence gaining significant attention in the reductive transformations of biomass-derived compounds [17].

Considering the cost-effectiveness, sustainability, and industrial reliance factor, several heterogeneous catalysts have been relentlessly proposed for catalytic transfer reduction processes. The catalytic reduction, including catalytic transfer hydrogenation (CTH), catalytic transfer hydrodeoxygenation (CTHDO), and catalytic transfer hydrogenolysis using IPA, is a promising yet challenging approach to scalable biofuel production. It requires a bifunctional acid-base catalyst, where the activation and adsorption of IPA occur. CTH of furfural, levulinic acid, HMF, and lignin model compounds have been carried out with suitably designed heterogeneous catalysts [21–24]. Several Lewis acid-based zeolites, metal phosphates, metal oxides, and metal-organic framework (MOF) have gained significant attention for CTH reactions [17]. He et al. reported an Al–Zr@Fe mixed oxide catalyst in the CTH of furfural to furfuryl alcohol with complete conversion and selectivity using 2-propanol [25]. Koehle et al. reported a Hf-modified Beta zeolite for the IPA-mediated MPV reduction of furfural [26]. Recently, an excellent activity in the CTH of levulinic acid to GVL was achieved using an acid-base bifunctional $ZrNPO_3$ catalyst [27]. Vasanthkumar et al. reported the CTH of vanillin, furfural, and levulinic acid to their corresponding alcohols using IPA and a nonprecious γ-Fe_2O_3 catalyst [28]. Atul et al. demonstrated synergistic participation of active sites in a Ni-Sn mixed-oxide catalyst in the IPA-mediated transfer hydrogenolysis of various lignin model compounds to their corresponding aromatic scaffolds [23]. Zhou et al. reported a multi-functional Cu-Re bimetallic catalyst for the CTHDO of furfural to 2-methyl furan with 94 % selectivity in IPA [29]. Similarly, $Ni_2P @ SiO_2$ with a yolk-shell structure has been reported by Li et al. in the CTHDO of vanillin to a mixture of MMP, alcohol, and other deoxygenated products [30]. There are numerous reports on the CTH reactions using IPA, but only a handful of reports are available for the CTHDO reaction. Moreover, most of the CTHDO reactions of vanillin have been carried out using precious Pd and noble metal-based catalysts with modulated acid sites [31–35]. The CTH reaction involves the simultaneous dehydrogenation of alcohols and the subsequent transfer of the produced hydrogen to the carbonyl group (C═O) of the target substrate. Whereas the CTHDO process involves the simultaneous dehydrogenation and hydrogenation steps along with an additional hydrogenolysis step. Due to the special catalytic requirement, it is challenging to achieve CTHDO, but the appropriate catalyst design with modulated acid sites can make the CTHDO process convenient. It has been reported that the cumulative effect of the Lewis and Bronsted acid sites with the Lewis base sites of the catalysts influences the CTHDO process by forming interfacial active hydrogen species. Thus, for the CTHDO of vanillin, only limited success has been achieved with the multi-functional and multi-metal-based catalysts having modulated acid-base surfaces.

MOFs have attracted attention in catalysis due to their structural and electronic modulation ability [20,36–38]. Their microporous framework provides high surface area and well-defined porosity. Moreover, they also offer an opportunity to fine-tune their high-valent metallic nodes and hence can exhibit outstanding acidic properties [39,40]. Zr-MOFs fall under this category and show excellent Lewis and Bronsted acid properties [41–43]. Zr-MOFs are excellent MPV catalysts in CTH reactions [44]. In this view, the role of metal node coordination and its modification has been explored for the MOF-808 by Valekar et al. in the CTH of furfural and HMF [45]. Among Zr-MOFs, UIO-66 is the most popular MOF due to its highly stable framework, the high charge density of the Zr_6O_8 SBU nodes, known for the potential Lewis acidity, and perceive the ability to tune the electronic properties by its structural

modulation [46,47]. The structural feature of UIO-66 is composed of alternatively μ_3 −OH. and μ_3 −O, and the high charge density of the Zr-O cluster is believed to be beneficial in the CTH process [47]. Recently, Qiu et al. reported the CTH of biomass-derived carbonyl compounds to their corresponding alcohols using UIO-66 [44]. Moreover, the coordinatively unsaturated open metal sites are often found in the framework structure of UIO-66 [48–51]. These coordinatively unsaturated open metal sites are either present naturally or can be induced deliberately by defect engineering. The coordinatively unsaturated open metal sites are formed when the metal nodes have low connectivity with the organic linker via the missing linker phenomena [48–51]. They served as the perfect Lewis centers and are found to be highly active in the catalytic process. Recently, Jiang et al. reported defect sites to regulate the structure-activity property and tuning the metal-support interaction in defect-rich Pd/ZrO_2 catalyst for the HDO of vanillin to MMP [52]. The UIO-66 is considered to be a proto-type MOF in defect engineering as it can maintain its structural stability despite the high number of defects. The role of the defect sites in the UIO-66 MOF was investigated in the synthesis of jet fuel precursors by Flor et al. [53]. Such defects in the UIO-66 framework can be made either by De Novo synthesis method or the post-synthesis method [54]. De novo synthesis route has been proven to be the best method for defect creation in UIO-66. De Novo synthesis method involves the use of either modulator, hemilabile linker, or a surfactant during the MOF synthesis to drive the defect creation.

Herein, a defect-enriched UIO-66 (designated as UIO-66$_{def}$) is reported for the selective CTHDO of vanillin to MMP. A surfactant-assisted strategy induces defects (cluster-missing) in MOF structure. Cetyltrimethylammonium bromide (CTAB), a cationic surfactant, was employed during the UIO-66 synthesis to synthesize defect-induced UIO-66. To our knowledge, it is the first report of CTHDO of vanillin to MMP using a MOF-based simple monometallic Zr catalyst. The outstanding CTHDO activity, characterizations & computational studies establish a deep understanding of the structure-activity relationship and underlying reaction mechanism.

2. Experimental

2.1. Materials

All chemicals were AR grade and were used without any further purification. Benzene dicarboxylic acid (BDC) was purchased from Sigma Aldrich. Zirconium chloride, dimethylformamide (DMF), hydrochloric acid, acetic acid, trifluoro acetic acid, 2-propanol, and vanillin were purchased from Merck Pvt. Ltd., India. Deuterated acetonitrile (CD_3CN) was obtained from TCI Chemicals (India) Pvt. Ltd.

2.2. Synthesis of UIO-66 and UIO-66$_{def}$

The UIO-66 was synthesized using the solvothermal method. 0.7 g of $ZrCl_4$ was dissolved in 30 mL of DMF. 30 mL DMF solution containing 0.5 g of BDC was added. Next, 10 mL of acetic acid and 0.15 g of HCl were added. The resultant solution was stirred for 30 min and transferred into a Teflon-lined autoclave for the hydrothermal treatment at 120 ℃ for 24 h. Finally, the white precipitate was washed with DMF and ethanol and dried in an oven at 80 ℃ overnight.

The UIO-66$_{def}$ was synthesized using a reported surfactant-assisted method [55]. 0.32 g of CTAB was added to the $ZrCl_4$ in DMF solution. The rest of the procedure was similar to the UIO-66 described above. After the synthesis, the CTAB was removed by a solvent extraction method (30 mL g^{-1}) using an aqueous solution of ammonium chloride (3 times).

2.3. Catalyst characterization

The detailed methods of catalyst characterization have been

included in the supplementary information (SI). A thorough investigation of the amount of defect elucidated by TGA is provided in SI and Table S1, which was supported by ^{1}H NMR (Fig. S1) with a detailed description.

2.4. Catalytic transfer hydrodeoxygenation of vanillin

The CTHDO of vanillin was carried out in a 15 mL autoclave. 1 mmol of the substrate, 40 mg catalyst, and 3 mL solvents were charged into an autoclave. The autoclave was then placed in an oil bath under stirring (600 rpm optimized to overcome the mass transfer) at 150 °C for 6 h. After the reaction, the catalyst was separated by centrifugation, and the reaction mixture was analyzed using a Shimadzu 2010 plus gas chromatography (GC) equipped with an FID detector and a BP-5 column (30 m × 0.25 mm × 0.25 μm). The products were confirmed using a GC-MS (Shimadzu GCMS 2030, Rtx-5 Sil Ms; 30 m × 0.25 mm × 0.25 μm). The vanillin conversion, yield, and selectivity were obtained using the expressions given below.

$$Vanillin\ conversion(\%) = \frac{moles\ of\ vanillin_{(initial)} - moles\ of\ vanillin_{(final)}}{moles\ of\ vanillin_{(initial)}} \times 100$$

$$MMP\ yield(\%) = \frac{moles\ of\ MMP\ formed}{moles\ of\ vanillin_{(initial)}} \times 100$$

$$MMP\ selectivity(\%) = \frac{MMP\ yield}{moles\ of\ vanillin_{(initial)}} \times 100$$
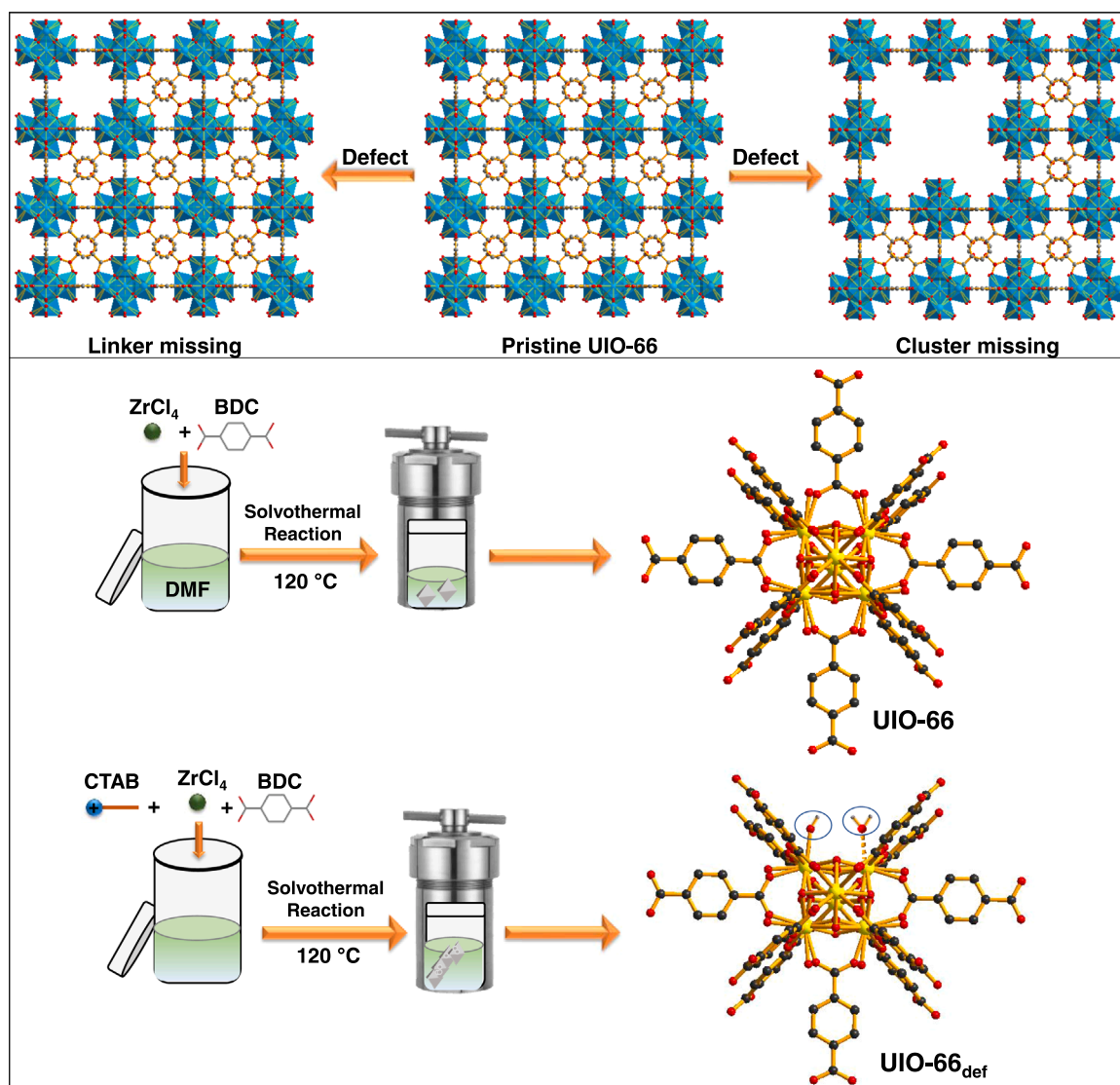
2.5. Computational methodology

The detailed methodology and computational details can be found in the SI.

3. Results and discussion

3.1. Catalyst synthesis and characterization

The crystal structure of UIO-66 has 12 connected hexameric Zr metal nodes ($Zr_6(μ_3\text{-}O_4)$ ($μ_3$-OH)$_4$) (Scheme 1). Each Zr_6 node binds up to 12 carboxylate groups of BDC linkers, and the removal of these BDC linkers generates under-coordinated, or unsaturated Zr sites, herein termed defect sites (Scheme 1). The defect sites can be generated either by the missing linker or the missing cluster using various synthesis

Scheme 1. Schematic presentation of the pristine UIO-66, defect induced via missing linker and missing cluster UIO-66 structures (top), and the synthesis of UIO-66 and UIO-66$_{def}$ (bottom).

methodologies discussed in the literature (Scheme 1, top) [47–50, 53–56]. The extent of the defect creation depends on the types of defects generated in the framework. The defect-induced unsaturated Zr sites remain coordinated with the hydroxyl group and atmospheric H_2O to maintain the framework charge balance (Scheme 1) [48–51]. The UIO-66$_{def}$ was synthesized to generate the excessive and efficient catalytic sites for the sustainable CTHDO of vanillin using IPA. The schematic presentation of the UIO-66$_{def}$ synthesis and the generated active sites are provided in Scheme 1.

The systematic formation of defects was evaluated using various characterization techniques. Fig. 1a provides the PXRD pattern of the UIO-66 and UIO-66$_{def}$, suggesting the crystallinity remained intact after the defect creation. The PXRD pattern of the UIO-66$_{def}$ exhibited a broad peak in the region of $2\Theta = 3$–7 ° corresponding to the **reo** nanoregion phase (Fig. 1a). The **reo** nanoregion arises due to the cluster defect, also termed a point defect in the MOF framework, and the observation is consistent with several earlier reports [55–57]. The cluster defect results in the deficiency of linkers from its ideal number, termed as missing linker, which is the actual cause of defect generation in UIO-66$_{def}$. The cluster defect resulting in missing linkers was further characterized using FT-IR (Fig. 1b). Before the FT-IR analysis, the samples were evacuated at 150 °C for 12 h to remove the interfering solvents in the spectra. The FT-IR spectra of UIO-66 and UIO-66$_{def}$ contain all the characteristic peaks of UIO-66 [46]. The -CO stretching frequency of the BDC linker appeared at 1663 cm^{-1}. However, the -CO peak intensity at 1663 cm^{-1} was broad and suppressed in UIO-66$_{def}$ (Fig. 1b). It indicates the disruption of the framework C=O bond and the creation of defects due to the linker deficiency by the addition of CTAB during synthesis, which is in good agreement with earlier reports of defect-induced UIO-66 [55,58]. In UIO-66$_{def}$, the linker vacancy generates unsaturated Zr defect sites, which are the potential source of extra framework physisorbed atmospheric water molecules and hydroxyl groups (Scheme 1) [58]. Hence, the UIO-66$_{def}$ contains a significantly broad peak in the region of 3000–3700 cm^{-1} than UIO-66 (Fig. 1b), which corresponds to the Zr−H_2O and μ_3 −OH., which are the source for the dynamic acidity in UIO-66$_{def}$ [59].

The high-resolution XPS analysis was carried out for UIO-66 and UIO-66$_{def}$ (Fig. 2a). The Zr 3d of UIO-66 exhibited two peaks at a binding energy of 183.1 eV for Zr 3d$_{5/2}$ and 185.4 eV for Zr 3d$_{3/2}$. However, the Zr 3d of UIO-66$_{def}$ showed slightly broad peaks with a positive shift of 0.4 eV towards higher binding energy than UIO-66 (Zr 3d$_{3/2}$ and Zr3d$_{5/2}$ appeared at 185.8 eV and 183.5 eV) (Fig. 2). The XPS peak broadening and shifting due to the change in the Zr-chemical environment in UIO-66$_{def}$ holds an agreement with the reported literature for defect-enriched MOF [53]. The O 1 s and C 1 s XPS spectra exhibited a similar trend of positive peak shift in UIO-66$_{def}$ due to the defect created by the missing

linker (Fig. 2b and Fig. S2). The O 1 s spectrum of UIO-66$_{def}$ deconvoluted to two peaks appeared at a binding energy of 530.5 eV and 532.5 eV, corresponding to Zr−O lattice oxygen and Zr-bonded oxygen of the carboxylate group (Zr−O−C) (Fig. 2b). Whereas in UIO-66, these peaks appeared at 532.1 eV and 530.2 eV. A similar trend of positive peak shift was observed for the C 1 s in UIO-66 and UIO-66$_{def}$ (Fig. S2).

The change in the porous architecture of the UIO-66$_{def}$ was estimated using an N_2 adsorption-desorption isotherm. UIO-66 and UIO-66$_{def}$ exhibited type-1 isotherm, suggesting their microporous framework (Fig. 3a, b). The BET surface area of UIO-66$_{def}$ was reduced to 1045 m^2/g from the BET surface area of 1269 m^2/g for UIO-66. A similar observation was found in several earlier reports where a decrease in the surface area was observed due to the defect generation upon linker missing from the framework [57,58]. The UIO-66$_{def}$ has a higher pore volume and larger pore diameter after the cluster-defect generation (Table 1). The comparable difference in the textural properties between the UIO-66 and UIO-66$_{def}$ suggests that the CTAB introduction during MOF synthesis agitated the self-assembly process of Zr nodes and BDC linker for the growth of crystal structure and prompted the generation of the unambiguously missing linker induced defect sites [57]. The defect/unit area for UIO-66$_{def}$ and UIO-66 was calculated to be 1.69×10^{-6} and 5.87×10^{-7} defect/m^2, respectively (SI for the detail).

The regular and well-defined octahedron surface morphology was observed for the UIO-66 (Fig. S3). However, in the presence of CTAB, the octahedron morphology was disturbed for UIO-66$_{def}$ (Fig. S3). HR-TEM analysis was conducted to gain more insight into the nanostructure of the UIO-66 and UIO-66$_{def}$ (Fig. 3c, d). The CTAB-mediated crystal growth in UIO-66$_{def}$ suggests that CTAB envelops the ligand sites while the Zr$_6$ nodes form and induce cluster defects. TEM image of UIO-66 exhibited well-separated octahedral morphology, whereas flat brick-like particles are stacked in one direction for UIO-66$_{def}$. In UIO-66$_{def}$, one face of one particle is stacked with one face of another, and those stacked faces would not be available for the N_2 adsorption in the surface area measurements. It is the reason the surface area was reduced for UIO-66$_{def}$ prepared by adding CTAB.

The TGA profiles of UIO-66 and UIO-66$_{def}$ provide the weight loss with temperature under aerobic conditions (Fig. 4a). The samples were activated in a vacuum under 100 °C before analysis to monitor the weight loss with temperature. Based on the TGA profiles of UIO-66 and UIO-66$_{def}$, it is suggested that the UIO-66$_{def}$ framework was less stable than the UIO-66 framework, which is in line with the previous report [50,55,56]. TGA analysis was conducted to estimate the number of missing linkers in UIO-66 and UIO-66$_{def}$, as reported by Shearer et al. [50]. The detailed methodology for the TGA analysis conducted in this study is provided in the SI. The normalized TGA curve for both UIO-66 and UIO-66$_{def}$ (Fig. 4a, b) suggests the desolvation and the dehydration
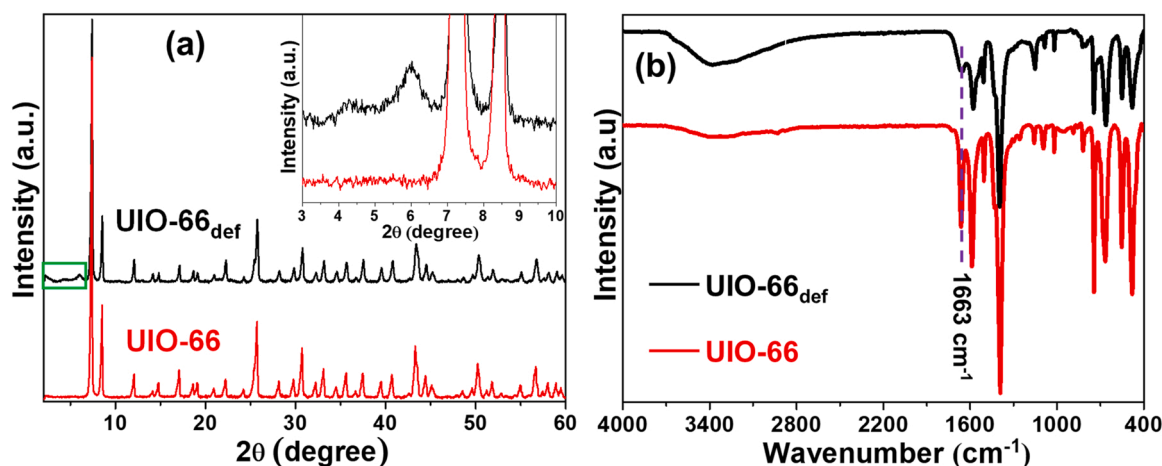

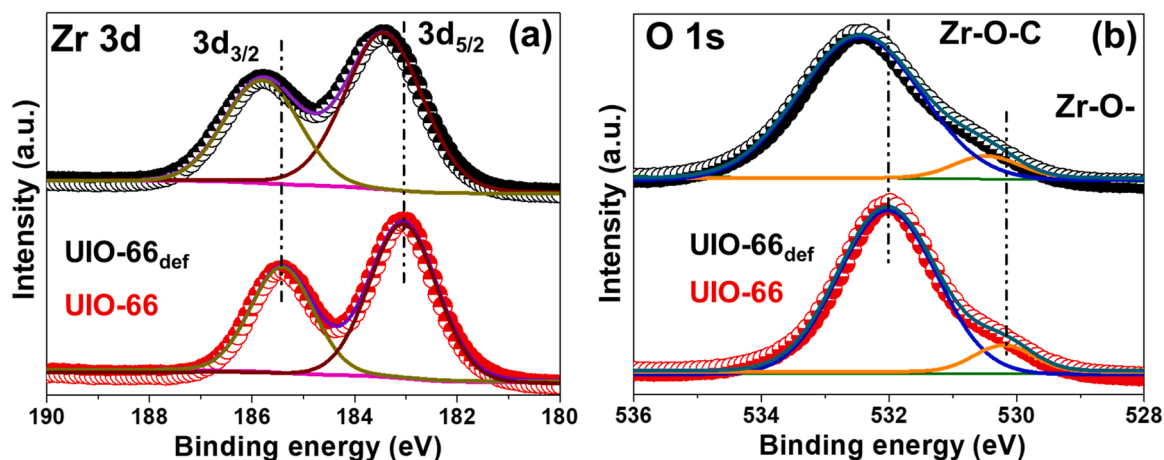**Fig. 1.** (a) PXRD patterns of UIO-66 and UIO-66$_{def}$ and (b) FT-IR spectra of UIO-66 and UIO-66$_{def}$.

Fig. 2. High-resolution XPS spectra of (a) Zr 3d of UIO-66 and UIO-66$_{def}$ and (b) O 1 s of UIO-66 and UIO-66$_{def}$.
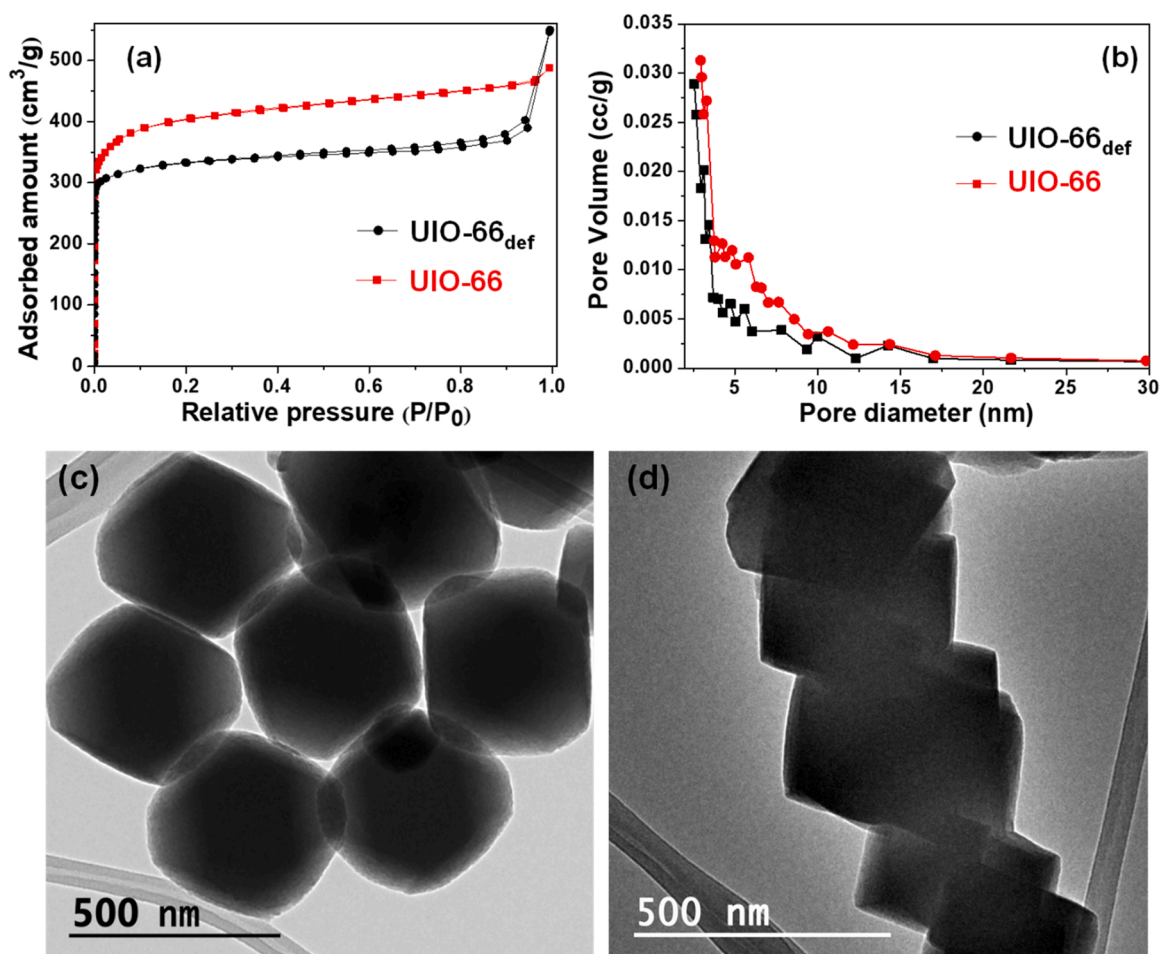

Fig. 3. (a) N$_2$ adsorption-desorption isotherms of UIO-66 and UIO-66$_{def}$, (b) pore size distribution of UIO-66 and UIO-66$_{def}$. HR-TEM images of (c) UIO-66 and (d) UIO-66$_{def}$.

of the framework Zr−OH$_2$ (defect-induced unsaturated Zr sites were coordinated to solvent molecules and atmospheric H$_2$O for the framework charge balance) occurred up to 280 °C for UIO-66 and 250 °C for UIO-66$_{def}$ respectively [50,56,57]. The subsequent weight loss due to the removal of the coordinated modulator (the acetic acid) and the dehydroxylation of the framework μ$_3$ −OH of the UIO-66 occurred in the range of 290 – 395 °C. The corresponding weight loss was observed in 260–375 °C for UIO-66$_{def}$. The final weight loss was due to the BDC

linker decomposition, which resulted in the formation of residual ZrO$_2$. Complete BDC decomposition occurred above 560 °C. The number of BDC linkers associated with each Zr$_6$ node was calculated from TGA analysis (SI). It can be seen from Table S1 that both the UIO-66 and UIO-66$_{def}$ exhibited 4.9 and 3.7 BDC linkers per ZrO$_6$ node in their respective framework. The high BDC linker deficiency in the UIO-66$_{def}$ framework is further understood by the magnitude of the weight loss trend in UIO-66$_{def}$, which was lower than the UIO-66 [56,57]. A similar

Table 1
Physicochemical properties of the synthesized Zr-MOF catalysts.

Catalyst	S_{BET} (m^2g^{-1})	Total pore vol. (cm^3g^{-1})	Avg. pore size (nm)	Acid sites $(\mu mol\ g^{-1})$	
				Weak acid (Temp.)	Moderate acid (Temp.)
UIO-66	1269	0.61	2.2	61.1 (170 – 320 °C)	14.3 (195 – 380 °C)
UIO-66$_{def}$	1045	0.72	2.8	132.3 (70 – 200 °C)	151.6 (210 – 390 °C)
[a]UIO-66$_{def}$	1035	0.71	2.6	–	–

[a] Spent catalyst.

observation was found in earlier reports [56,57]. Moreover, the dissolution ^{1}H NMR was also carried out for UIO-66 and UIO-66$_{def}$ to estimate the molar ratio of acetate (modulator) to BDC linker (Fig. S1). The detailed procedure and analysis method are discussed in SI. The molar ratio of acetate to BDC for UIO-66$_{def}$ was higher than UIO-66, suggesting the lower number of BDC accommodated in UIO-66$_{def}$, due to which, a greater number of acetate modulators were incorporated to maintain the charge balance for the framework integrity. The missing linker per Zr$_6$ node further satisfy from the dissolution ^{1}HNMR analysis and support the TGA observation. Based on all the above characterization analyses, it is concluded that the BDC linker deficiency was the primary reason for the defect centres in the UIO-66$_{def}$.

The unsaturated Zr sites were generated due to missing linkers in UIO-66$_{def}$, which are the epitome of the Lewis acid sites. The framework μ_3 −OH contributes to the weak Bronsted acidity, while the charge-balancing fluxional Zr−OH, Zr−OH$_2$, at the defect sites are regarded as the dynamic acid sites or the strong Bronsted acid sites in the UIO-66$_{def}$ [51,53,56,60]. Hence, to evaluate the comparative acidity between the UIO-66 and the UIO-66$_{def}$, an NH$_3$-TPD analysis was conducted. Catalytic reactions were conducted under mild conditions; thus, the acidity in the lower temperature was important and considered here. Both samples showed broad NH$_3$ desorption (Fig. 4c). The deconvoluted NH$_3$-TPD profiles for the UIO-66 and UIO-66$_{def}$ suggest the nonlinear NH$_3$ desorption occurred due to the hetero-acidic sites in their frameworks (Figs. 4c & S4). The UIO-66 showed a comparatively weaker TCD signal in the range of 180–350 °C than the UIO-66$_{def}$, suggesting the higher acidic nature of the UIO-66$_{def}$ [39,61,62]. A relatively strong and modified NH$_3$-TPD profile was observed for UIO-66$_{def}$ in the range of 190–390 °C. The TCD signal shifted towards a higher temperature, suggesting that the adsorbed NH$_3$ exhibited stronger interaction with the stronger acidic sites of UIO-66$_{def}$. Moreover, the broad and intense NH$_3$ desorption signal for UIO-66$_{def}$ could be due to the greater residence time of NH$_3$ molecules near the defect sites in UIO-66$_{def}$ than the undefective sites in UIO-66. The weak NH$_3$ desorption signal in UIO-66 arises as the NH$_3$ molecule only forms the framework μ_3 −OH—NH$_3$ and Zr—NH$_3$ type interactions, while in UIO-66$_{def}$, in addition to these interactions, the NH$_3$ molecule forms stronger interactions near the defect sites with the defect induced unsaturated Zr—NH$_3$ and Zr−OH—NH$_3$ type interactions. Hence, the UIO-66$_{def}$ exhibited a stronger and modified NH$_3$ desorption signal than the UIO-66. The comparative acidic strength and the total NH$_3$ desorption for UIO-66 and UIO-66$_{def}$ are summarized in Table 1. The UIO-66$_{def}$ showed 1.6 times higher acidity than UIO-66 based on the amount of NH$_3$ desorbed per defect site (Details in SI).
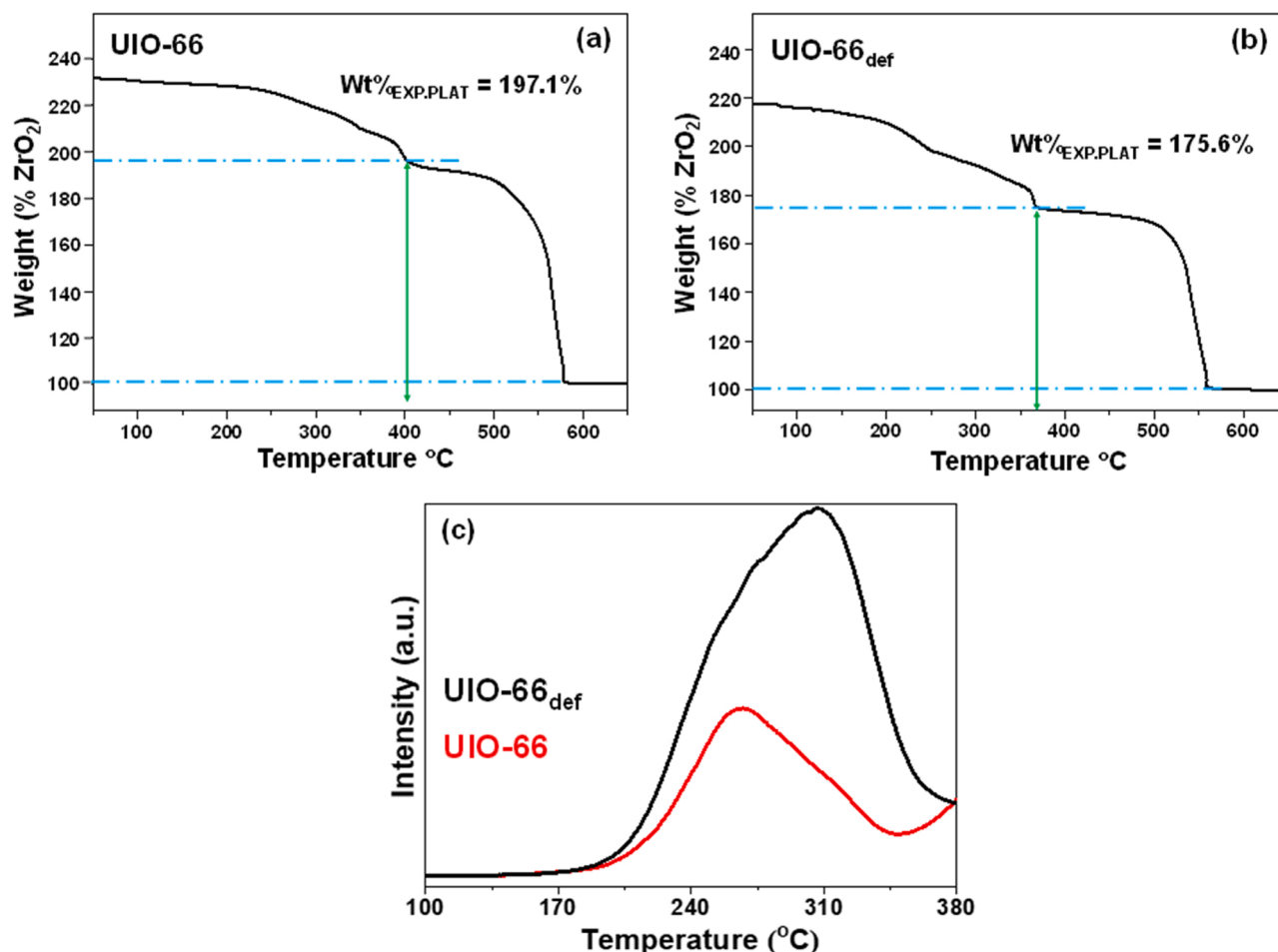

Fig. 4. TGA curves of (a) UIO-66, (b) UIO-66$_{def}$ and (c) NH$_3$-TPD profiles of UIO-66 and UIO-66$_{def}$. (Deconvoluted profiles are presented in Fig. S4).

The acidic character of UIO-66 and UIO-66$_{def}$ was further assessed by the drift FT-IR analysis using the CD$_3$CN as a probe molecule. The samples were degassed at 120 °C with Ar flow (20 mL min^{-1}) in the FT-IR chamber for 2 h prior to analysis to remove the interfering species and then saturated with the CD$_3$CN. The chemisorption analysis of CD$_3$CN was monitored by its desorption with temperature. After the CD$_3$CN was introduced into the drift cell, the temperature was kept at 50 °C and increased with a heating rate of 2 °C min^{-1} in Ar flow (10 mL min^{-1}). The FTIR spectra were recorded every 10 °C from 50 °C to 120 °C (Fig. 5a, b). It can be seen that the desorption pattern of CD$_3$CN was observed in the region of 2400–2200 cm^{-1} for the ν(CN) vibrational bands. Three bands observed at 2360, 2277, and 2261 cm^{-1} are attributed to CD$_3$CN adsorption on Lewis acid sites, Bronsted acid sites, and physically adsorbed CD$_3$CN, respectively. The UIO-66 exhibited only a band attributed to the physically adsorbed CD$_3$CN, and the band got quickly vanished upon increasing the temperature, which signifies that the binding of CD$_3$CN with the UIO-66 was weak. However, in the case of UIO-66$_{def}$, the band associated with the physically adsorbed CD$_3$CN got reduced with increasing temperature. A strong band at 2277 cm^{-1} attributed to the Bronsted acidic sites started to appear and become sharpened on increasing the temperature, signifying the strong interaction of CD$_3$CN with the dynamic Bronsted acid sites due to the framework μ_3 −OH moieties and the fluxional Zr−OH and Zr−OH$_2$. Similarly, a weak adsorption band appeared at 2360 cm^{-1} attributed to the CD$_3$CN interaction with the Lewis acid sites. It can be seen that the vibrational band attributed to the CD$_3$CN adsorption on the Lewis acid sites is relatively weaker, which is consistent with recent literature [53, 63]. However, such bands are absent in UIO-66, which suggests the defect generation effectively created the variable acidic sites that are the catalytic sites. Moreover, the drift analysis using IPA as the probe molecule was also conducted to estimate the degree of IPA activation in UIO-66 and UIO-66$_{def}$. Initially, the IPA was adsorbed on UIO-66 and UIO-66$_{def}$, and its desorption extent with temperature was monitored using drift analysis. Similar to CD$_3$CN drift analysis, after IPA adsorption, the temperature was increased from 50 °C to 90 °C and the desorption pattern of IPA was recorded (Fig. S5). Spectra show that IPA was less efficiently adsorbed on UIO-66 than UIO-66$_{def}$. The ν_{as}(CH$_3$) band of IPA was distinctly split and remained adsorbed on UIO-66$_{def}$ to a greater extent than UIO-66, suggesting the IPA molecule efficiently chemisorbed on the UIO-66$_{def}$ due to the defect-induced framework structure [64].

3.2. Catalytic activity

3.2.1. CTHDO of vanillin over UIO-66 and UIO-66$_{def}$

Selective catalytic hydrodeoxygenation (CHDO) of Ar−CHO to Ar−CH$_3$ with its preserved aromatic structural motif under a sustainable reaction condition is challenging chemistry for the lignin-derived platform chemicals. Vanillin is a significant component in lignin pyrolysis oil. The CHDO of vanillin to 2-methoxy-methyl phenol (MMP), a potential biofuel, is often achieved under high H$_2$ pressure with noble metals or transition metal-based catalysts (Scheme 2). The vanillin hydrodeoxygenation to MMP proceeds through sequential hydrogenation and hydrogenolysis with H$_2$ (Scheme 2). The carbonyl group of vanillin hydrogenates to vanillyl alcohol, followed by the hydrogenolysis of the vanillyl alcohol to form MMP (Scheme 2). However, the CTHDO of vanillin to MMP is a sustainable route, where the MMP can be achieved without using the external H$_2$ but with alcohol as an indirect 'H' source (Scheme 2). In CTHDO of vanillin, the first step involves the hydrogen transfer from the IPA to the carbonyl group of vanillin to form vanillyl alcohol. The resultant vanillyl alcohol immediately undergoes etherification with IPA to produce 4-(isopropoxymethyl)− 2-methoxyphenol (ether intermediate). In some instances, the vanillyl alcohol cannot be isolated and instantly convert to ether intermediate due to the surface acidity of the catalyst. Finally, the hydrogenolysis of the ether intermediate occurs to form MMP. The former pathway employing H$_2$ requires noble metals or transition metals loaded on suitable supports, wherein metals assist in the dissociative adsorption of H$_2$ and support assists in the adsorption of vanillin. On the contrary, the CTHDO requires a suitable modulated acidic surface for the co-adsorption and activation of the vanillin and IPA. The vanillin adsorption occurs via C═O of the carbonyl group on the high valent Lewis metal sites (Zr^{+4}, Sn^{+4}, Ni^{+2}, etc.). At the same time, IPA also adsorbs and undergoes MPV reduction to transfer the H to the carbonyl group of the vanillin. The vanillyl alcohol immediately reacts with the alcohol and converts to the corresponding ether. Finally, the ether hydrogenolysis to MMP occurs due to the surface acidity of the catalyst.

Herein, the CTHDO of vanillin was carried out using the UIO-66 and the UIO-66$_{def}$ with IPA, and the catalytic data is presented in Table 2a. It can be seen that the UIO-66 exhibited only 7.6 % of the vanillin conversion to 4-(isopropoxy methyl)− 2-methoxyphenol (ether intermediate), and no MMP was formed (Entry 1, Table 2a). However, vanillin was exclusively converted to MMP (100 % selectivity) using UIO-66$_{def}$ under the specified reaction conditions (Table 2a, footnote). It suggests that UIO-66 doesn't contain the required active sites for the CTHDO of vanillin and hence is not a suitable CTHDO catalyst.

The reactivity of vanillin CTHDO over UIO-66$_{def}$ greatly depended on the reaction temperature and time. Moreover, the MMP and intermediate ether selectivity depended on the reaction time and temperature. Thus, it was crucial to establish the vanillin reactivity with time and temperature to justify the active sites of the UIO-66$_{def}$. Initially, the reaction was carried out at 90 °C and afforded only 4.3 % vanillin conversion after 24 h. Although a moderate vanillin conversion (44.2 %) was obtained at 100 °C after 24 h, the MMP formation was not achieved
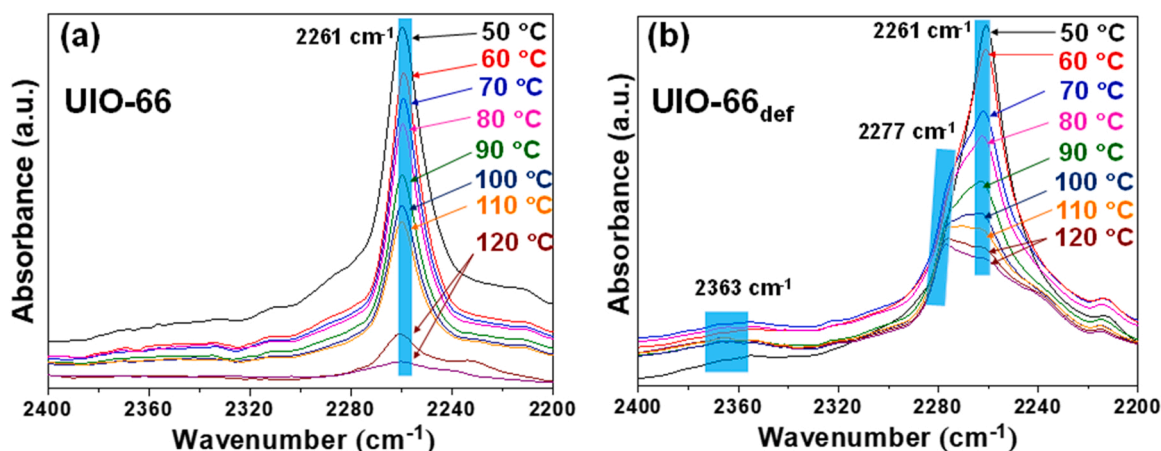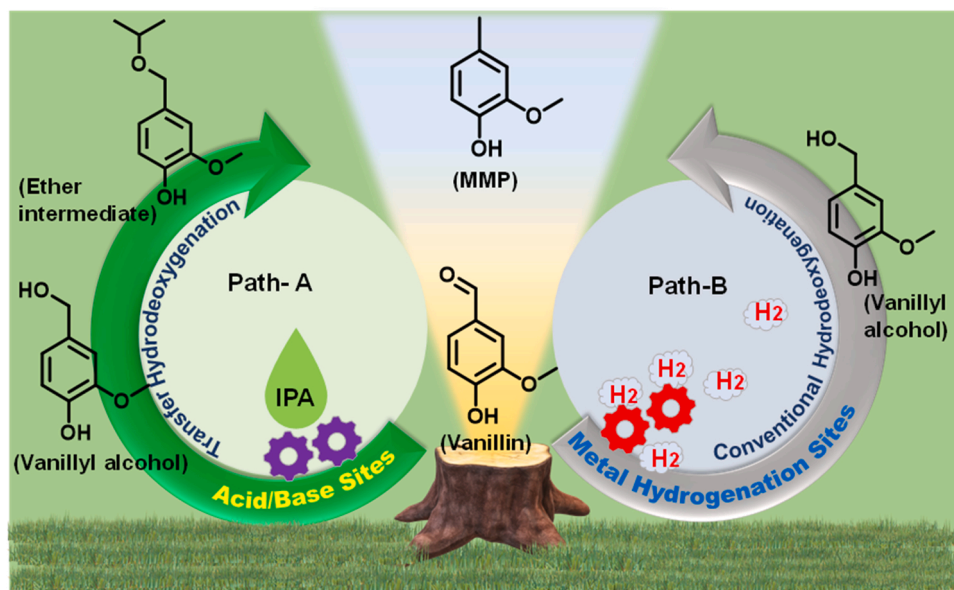

Fig. 5. CD$_3$CN drift FT-IR spectra of (a) UIO-66 and (b) UIO-66$_{def}$.

Scheme 2. Possible routes of vanillin hydrodeoxygenation.

Table 2
Catalytic activity and adsorption energies data.

(a)	CTHDO of vanillin using IPA.			
Entry	Catalyst	Conversion (%)	Ether selectivity (%)	MMP selectivity (%)	TOF (h^{-1})
1	UIO-66	7.6	100	0	$(0.04)^a$, $(0.23)^b$, $(0)^{c,e}$ $(2.24)^d$
2	**UIO-66$_{def}$**	**99.9**	**0**	**~100**	$(0.47)^a$, $(1.26)^{b,c}$ $(7.67)^{d,e}$

Reaction condition: Vanillin (1 mmol), catalyst (50 mg), temperature (150 ºC), time (9 h), IPA (3 mL). TOF = Moles of vanillin converted per mole of Zr per hour.[a]Calculated based on the total Zr present in the catalyst.[b]Calculated based on active Zr sites present in the catalyst deduced from TGA.[c] TOF = Moles of MMP formed per mole of Zr per hour, and it was calculated based on active Zr sites present in the catalyst deduced from TGA.[d]TOF based on NH_3-desorbed = Moles of vanillin converted per moles of NH_3 desorbed from the sample per hour.[e]TOF based on NH_3-desorbed = Moles of MMP formed per moles of NH_3 desorbed from the sample per hour. TOF values are also calculated at lower vanillin conversions and presented in Table S2 of SI)

(b)	Individual and co-adsorption energies of IPA and vanillin on UIO-66 and UIO-66$_{def}$.		
System	Adsorption energy (eV)	Systems	Adsorption energy (eV)
UIO-66 + IPA	-0.47	UIO-66$_{def}$ + IPA	-1.28
UIO-66 + vanillin	-0.10	UIO-66$_{def}$ + vanillin	-1.43
UIO-66 + IPA + vanillin	-0.90	UIO-66$_{def}$ + IPA + vanillin	-2.85
-	-	UIO-66$_{def}$ + acetone	+ 5.26

even after 24 h (Fig. 6). It is because, at a lower temperature, the defect-induced Zr sites are blocked by the charge-balancing atmospheric H_2O molecules and anions, which can be removed at the elevated temperature (>100 ºC) to generate reactive unsaturated Zr sites. At an elevated temperature, the unsaturated Zr^{+4} sites become available for catalytic reaction; hence, vanillin conversion was achieved at elevated temperatures (> 100 ºC) (Fig. 6). At 110 ºC, the vanillin conversion was 18.2 % after 3 h, but no MMP was obtained. The vanillin conversion improved by increasing the time and reached 72.8 % with almost complete ether selectivity after 24 h (Fig. 6). At this temperature, only ether intermediate was obtained, and no vanillyl alcohol was found in the reaction mixture, which indicates that as soon as the vanillin converted to vanillyl alcohol, it immediately converted to ether by reacting with IPA. The vanillin conversion relatively improved at 120 ºC compared to 110 ºC and the complete vanillin conversion was achieved after 24 h with a very low selectivity of MMP (7.1 %). It indicates that MMP production relies much on temperature. The vanillin reactivity under all the reaction temperatures was evaluated with time (Fig. 6). Next, the reaction was conducted at 130 ºC, and complete vanillin conversion was achieved within 9 h with the MMP selectivity of 22.8 %. To obtain better MMP selectivity, the reaction time was extended to 24 h, and the MMP selectivity could only improve to 34.2 %. It suggests that the MMP production was not favourable below 130 ºC. At 140 ºC, the vanillin conversion was 73.2 %, and MMP selectivity was 28.3 % after 3 h. On extending the reaction time from 3 h to 24 h, the MMP selectivity was improved to 80.2 % (Fig. 6). The remarkable enhancement in the vanillin conversion and MMP selectivity occurred at 150 ºC, indicating the required reaction site activated at this temperature to convert ether to MMP. At 150 ºC, the vanillin conversion and MMP selectivity achieved 90.5 % and 57.3 %, respectively, in 3 h. When the time was extended to 6 h, the MMP selectivity increased to 81.9 %, and complete MMP selectivity was achieved after 9 h (Fig. 6). Fig. S6 shows the reaction profiles for 1–6 h at different temperatures (100 ºC-150 ºC). The reaction was further conducted at 160 ºC to reduce the time duration for MMP production. But it was found that no significant improvement in MMP production was achieved at this temperature. The catalytic activity data demonstrates the revolutionary emanation of the catalytically active sites for MMP production at elevated temperatures.

According to the temperature-time relation at 150 ºC and 160 ºC for 0.5–1.5 h, it was found that, after 0.5 h, the vanillin conversion was 28.7 % with 9.6 % MMP selectivity at 150 ºC, and the vanillin conversion was slightly increased to 30.8 % with 10.4 % MMP selectivity at 160 ºC (Fig. S7a, b). It can be seen from the plot that the MMP selectivity exhibited almost a similar trend irrespective of temperature between 150 ºC and 160 ºC. The temperature-time correlation plots in Fig. 6 and Fig. S7a,b suggest that the vanillin conversion and MMP selectivity depend on the temperature and time up to 150 ºC. At all temperatures, the vanillin conversion was achieved, but the MMP selectivity was restricted irrespective of the reaction time when the temperature was
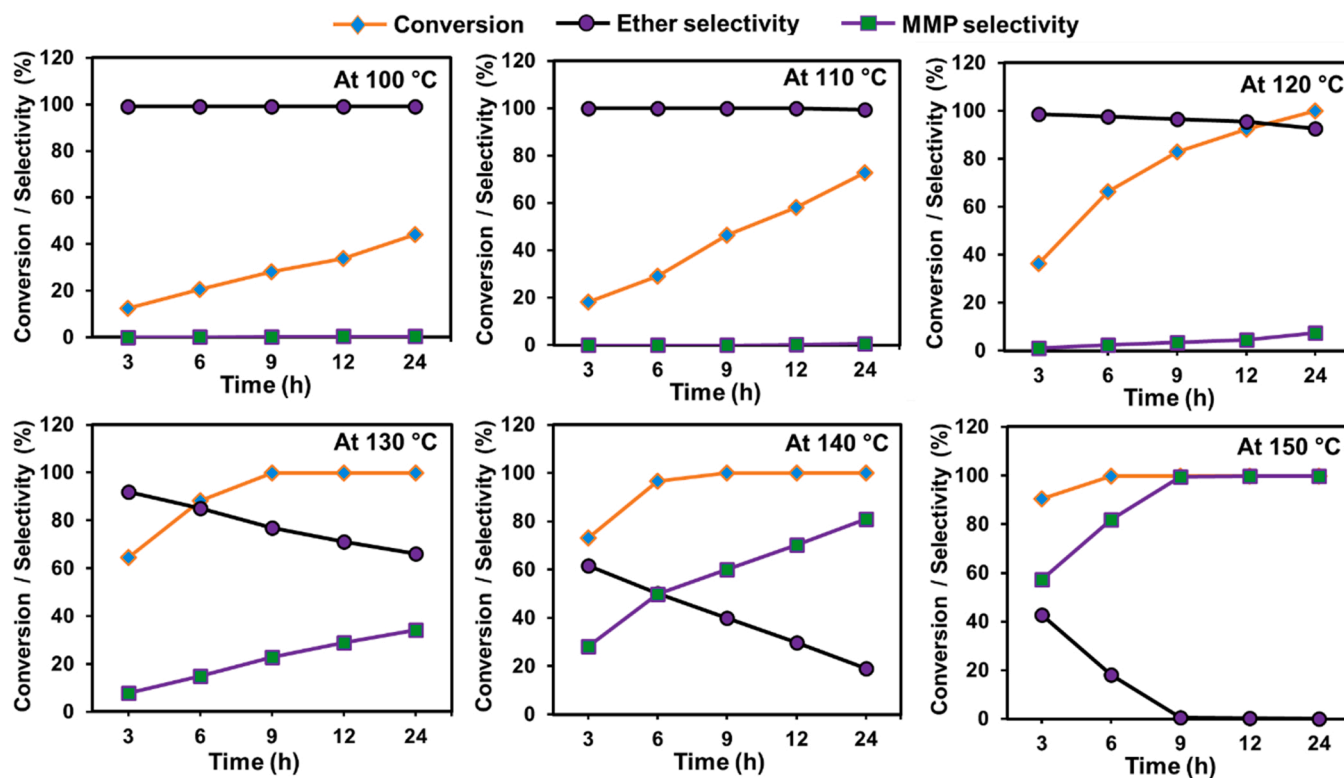
Fig. 6. Influence of temperature and time for vanillin reactivity over UIO-66$_{def}$. (Reaction condition: Vanillin (1 mmol), catalyst (50 mg), IPA (3 mL)).

below 140 ºC. At 150 ºC or 160 ºC, the complete vanillin conversion occurred quickly, but the MMP production increased steadily and required 9 h to achieve nearly 100 % selectivity. Hence, the 150 ºC temperature and 9 h reaction time were chosen as appropriate reaction conditions for the CTHDO of vanillin. Moreover, no other by-product was obtained even at higher temperatures and prolonged reaction time, suggesting that the MMP production is specific under the CTHDO reaction route using UIO-66$_{def}$. The optimization of the UIO-66$_{def}$ amount (20–50 mg) for the CTHDO of 1 mmol vanillin was conducted (Fig. S7c). 50 mg UIO-66$_{def}$ was found to be the optimized catalyst amount for 1 mmol of vanillin. As mentioned in the above section, the UIO-66$_{def}$ contains the discrete nature of acid sites whose concentration is directly proportional to the amount of UIO-66$_{def}$ present in the reaction mixture. Hence, the vanillin conversion and MMP selectivity depend on the amount of UIO-66$_{def}$.

The experimental results conclude that the vanillin to MMP transformation occurs via ether intermediate in a consecutive manner over UIO-66$_{def}$. Therefore, the kinetics of individual steps were studied for vanillin to ether and ether to MMP transformations, respectively. Based on our experimental study and obtained results, it can be concluded that MMP production from ether intermediate did not proceed below 120 °C. Therefore, the temperature ranges from 100 °C to 120 °C were chosen for the first-step conversion, i.e., vanillin to ether, and temperature ranges from 130 °C to 150 °C were chosen for the second-step conversion, i.e., vanillyl ether to MMP. Due to an excess amount of isopropanol in the reaction, the rate of individual steps is independent of the concentration of isopropanol. Therefore, the conversion of vanillin to ether and ether to MMP follows the first-order rate law. The rate of the individual step was calculated from the slopes obtained from the ln (1 − x) vs time at different temperatures. The activation energies for vanillin to ether and ether to MMP transformation were calculated by Arrhenius plot using ln k(obs) vs 1/T shown in Figs. S8 & S9. The results revealed a higher activation energy barrier for ether to MMP (207.0 kJ mol^{-1}) than vanillin to ether (71.8 0 kJ mol^{-1}) transformations, suggesting that the C-O bond dissociation of ether during transfer hydrodeoxygenation is

the rate-determining step (results are also consistent with conclusion obtained by theoretical study) for vanillin to MMP transformation using IPA. From the Arrhenius plot, the activation enthalpy (ΔH), and free energy of activation (ΔG) were calculated for vanillin to ether and ether to MMP transformations at temperatures 393 K and 408 K, respectively. The activation enthalpy and free energy of activation were determined using (ΔH = Ea − RT) and (ΔG = −RT ln (NAhk/RT)) respectively, where R is the gas constant (8.314 Jmol^{-1}K^{-1}), T is the temperature (k), NA is Avogadro's number (6.022 × 10^{23}), h is Planck's constant (6.626 × 10^{-34} m^2 kg/s), and k is rate constant. The values of Ea, ΔH, and ΔG were calculated to be 71.8 kJ mol^{-1}, 68.5 kJ mol^{-1}, and 19.7 kJ mol^{-1} for vanillin to ether transformation and 207 kJ mol^{-1}, 203.5 kJ mol^{-1}, and 89.58 kJ mol^{-1} for ether to MMP transformation, respectively.

The comparative catalytic data presented in Table S3 suggest that the vanillin CTHDO requires transition or noble metal active sites other than the framework metal. In the present study, only framework Zr sites exhibited excellent activity after creating defects in the UiO-66 framework.

3.2.2. Mechanistic investigation

It is imperative to understand the nature of the active sites present in UIO-66$_{def}$ and correlate their influence on the catalytic activity to understand the CTHDO mechanism over UIO-66$_{def}$. The detailed investigation of vanillin CTHDO over the Zr nodes has not been discussed. Hence, in this study, we unravel the active sites of UIO-66$_{def}$ influencing the catalytic performance of the CTHDO of vanillin. The CTHDO involves the synergistic activation of IPA and vanillin on the acid sites; hence, based on the CD$_3$CN & IPA drift FT-IR, and NH$_3$-TPD analysis results, it is proposed that the defect-induced acid sites in UIO-66$_{def}$ catalyze the CTHDO process. The local structure of the UIO-66$_{def}$ possesses the frustrated Lewis pair (unsaturated Zr sites and Zr−OH. sites) and is suitable for the co-adsorption of vanillin and IPA [45,47]. The defect-induced unsaturated Zr sites act as Lewis acid sites to polarize the C═O bond of vanillin and the Zr−OH groups act as active centres to adsorb and activate IPA. The synergy consequences in the simultaneous

dehydrogenation of IPA and hydrogenation of the C=O of vanillin by following the MPV route (Hydrogen transfer route), reported by Sitti-wong *et al.*, 2021 and Valekar *et al.*, 2020, wherein the CTH of furfural with IPA has been proposed [45,46]. However, it is noted that we didn't trace the occurrence of vanillyl alcohol (C=O hydrogenation product of vanillin) in the reaction mixture. It is because of the fast etherification between the short-lived in-situ generated vanillyl alcohol and IPA, which occurs on acidic support [65]. A control experiment was conducted to validate the observation. The vanillyl alcohol reacted with IPA under the optimized temperature conditions. Vanillyl alcohol was instantly converted to ether intermediate in less than 10 min. It is because the UIO-66$_{def}$ carries the unsaturated Zr sites with dynamic acidity, which reinforces the fast etherification reaction. The defect centers in UIO-66$_{def}$ not only provide the required diffusion channels but also imparts the emerging surface acidity for polarizing the C–O bond of ether molecule for its hydrogenolysis to MMP. The influence of unsaturated Zr sites as the Lewis acid and the μ_3 –OH and Zr–OH as the dynamic acid, or Bronsted acid in the CTHDO of vanillin was validated by performing the poisoning test. In the poisoning experiment, the emerging Lewis acid sites and Bronsted acid sites were passivated with pyridine and 2,6-lutidine as the probe molecules, respectively [27,66]. The CTHDO reaction was significantly affected by pyridine (Fig. 7a). Pyridine passivates both acid sites, i.e., Lewis Zr sites and Bronsted acid sites; hence, it failed to adsorb vanillin, which is the primary step in the CTHDO reaction. On increasing the pyridine concentration in the reaction mixture from 10 μL to 40 μL, the vanillin conversion and MMP selectivity decreased (Fig. 7a). Pyridine causes severe poisoning in vanillin conversion. When the pyridine concentration reached 40 μL, the vanillin conversion seized. The effect of the vanillin conversion and the MMP selectivity was studied in different amounts of 2,6-lutidine (Fig. 7b). The vanillin conversion was not much influenced by the addition of 2,6-lutidine; however, the MMP selectivity was drastically lowered. It is due to the selective passivation of the Bronsted acid sites in the MOF framework by the 2,6-lutidine [27,66]. The MMP selectivity significantly dropped on increasing the 2,6-lutidine amount, which signifies that the etherification and the hydrogenolysis were promoted by the Bronsted acid sites of the catalyst (Fig. 7b). Hence, it is concluded that both the Lewis acid and Bronsted acid are imperative for the CTHDO of vanillin to MMP. The Zr Lewis acid sites mainly catalyze the vanillin hydrogenation, and the Bronsted acid sites promote the etherification and hydrogenolysis steps. DFT studies were conducted to validate the experimental observations, and the comparative CTHDO activity was computed for the UIO-66 and UIO-66$_{def}$.

3.2.3. DFT study

The optimized structures for the UIO-66 and UIO-66$_{def}$ are provided in Fig. S10. However, for straightforward interpretation, the

representative structures for the optimized structures of the UIO-66 and UIO-66$_{def}$ are shown in Fig. 8. The CTHDO activity was estimated by considering the adsorption of IPA and vanillin on UIO-66 and UIO-66$_{def}$. The IPA and vanillin molecules were added to Zr1 and Zr2 sites of the UIO-66 and optimized (Fig. S11). The UIO-66$_{def}$ structure was formed by removing the ligand attached to Zr1 and Zr2 atoms in the pristine MOF structure and adding a –OH and H$_2$O moiety to the Zr1 and Zr2 sites (Fig. 8). However, during adsorption analysis for the defective structure, the water molecule was removed, the vanillin molecule was adsorbed at the vacancy site Zr2, and IPA was adsorbed near the –OH attached to Zr1 atom. First, the individual and co-adsorption of vanillin and IPA on the UIO-66 and UIO-66$_{def}$ systems were computed, and the corresponding adsorption energies are provided in Table 2b. The possibility of the back hydrogenation of the dehydrogenation product of IPA, i.e., acetone to IPA over UIO-66$_{def}$, is ruled out, which was verified by acetone adsorption on UIO-66$_{def}$. The positive adsorption energy value suggested acetone adsorption on UIO-66$_{def}$ is energetically unfavourable (Table 2b, Fig. S12). More negative adsorption energies for the UIO-66$_{def}$ indicate enhanced catalytic performance compared to the UIO-66. Mulliken charges of the atoms corresponding to the stronger interaction regions (as indicated by the bonds in Fig. S11a and b) within the isolated molecules and co-adsorbed systems are provided in Tables S4 and S5 [67]. The extent of the adsorption of IPA and vanillin with the UIO-66$_{def}$ can be further understood by their closet occupancy after the structure optimization than UIO-66 (Fig. S11 and Fig. 9). The optimized structures are presented in Fig. 9 for easy interpretation. The carbonyl group of the vanillin makes interaction with a length of 2.63 Å with the Zr2 of the UIO-66. However, the interaction becomes stronger in UIO-66$_{def}$ with an interaction distance of 2.24 Å (Fig. 9a and b). Similarly, the hydroxyl hydrogen of IPA also strongly interacts with the Zr1–OH and μ_3 –OH groups with interaction distances of 1.51 Å and 1.78 Å (Fig. 9b). In UIO-66, IPA interaction occurred with an interaction distance of 1.95 Å and 2.50 Å, suggesting the IPA interacts intently with the UIO-66$_{def}$. Moreover, the partial negative and positive charges of the atoms increased after co-adsorption, indicating the enhanced polarity of the molecules forming the non-covalent bonds at the interaction sites. Interestingly, the change in the Mulliken charge distribution is more prominent in UIO-66$_{def}$ than in UIO-66. The adsorption energies for the UIO-66$_{def}$ were more negative and feasible than the UIO-66 structures, suggesting a stronger interaction occurred for the vanillin and IPA with the UIO-66$_{def}$ (Table 2b). The UIO-66 experienced weak adsorption of vanillin, which is consistent with the catalytic activity data presented in Table 2a, suggesting the structural features of the UIO-66 is not suitable for vanillin conversion. It ensures enhanced catalytic performance of the system after defect formation in UIO-66$_{def}$. With this idea, computational investigation of the reaction mechanism for the CTHDO of vanillin using IPA was explored for both UIO-66 and UIO-66$_{def}$. The
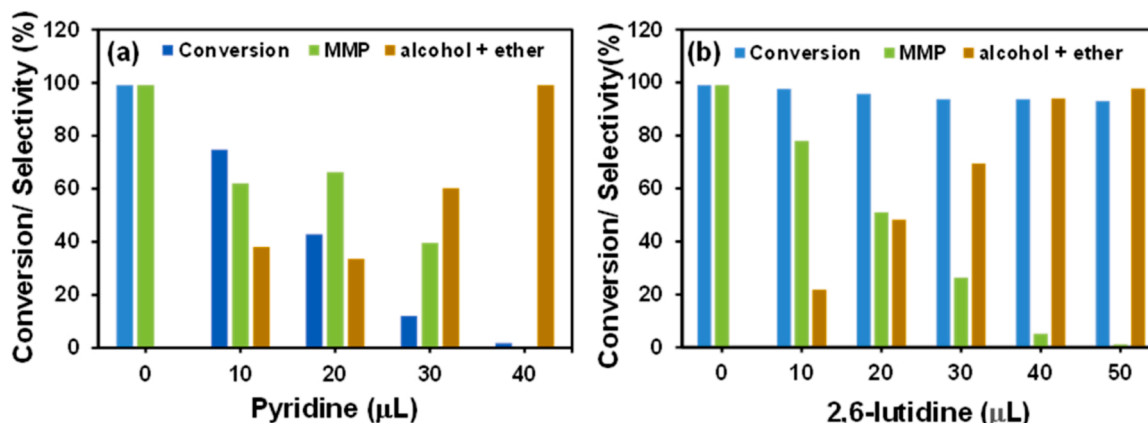
Fig. 7. Poisoning test using (a) pyridine and (b) 2,6 lutidine in the CTHDO of vanillin using UIO-66$_{def}$.
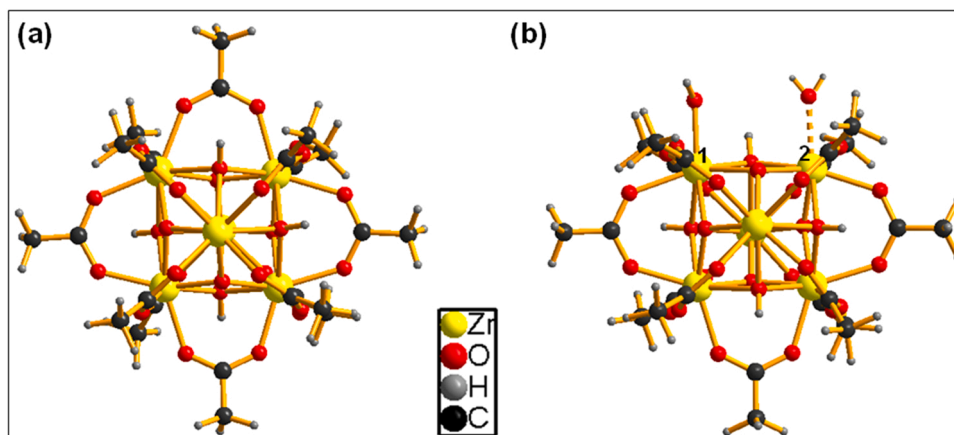
Fig. 8. The representative structure for the optimized system of (a) UIO-66 and (b) UIO-66$_{def}$. (For convenience, the carboxylate groups have been substituted by acetate groups) (the optimized structures are presented in Fig. S10).
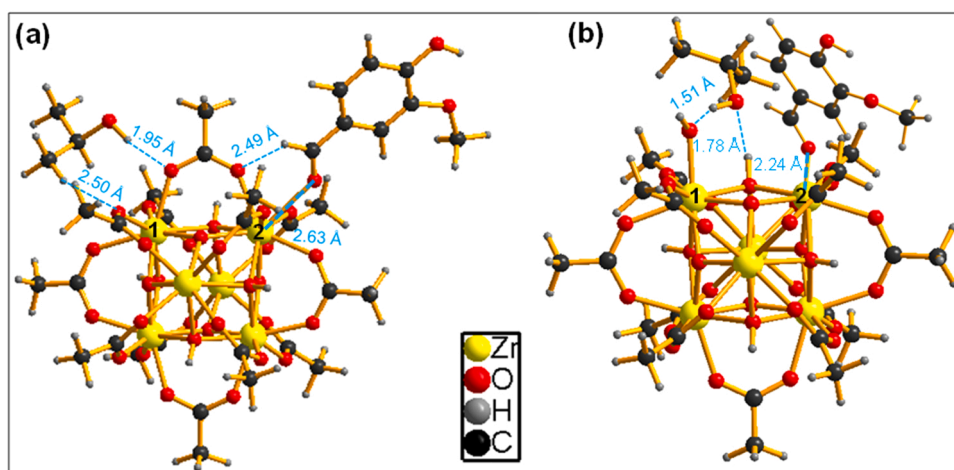

Fig. 9. Representative structure of vanillin and IPA co-adsorbed on (a) UIO-66 and (b) UIO-66$_{def}$ structures. (The optimized structure and atom respected atom notations are provided in Fig. S11).

corresponding free energy profile corresponding to UIO-66 and UIO-66$_{def}$ is provided in Fig. S13 and Fig. 10. Free energies of each complex structure corresponding to each reaction step (denoted as reaction coordinates) are calculated as the difference between the absolute free energy of the complex and the sum of the free energies of the components constituting the complex, as explained in the computational methodology section in the SI [68]. The complete optimized structures of the reaction coordinates and their corresponding components are provided in Table S6 and Table S7 for UIO-66$_{def}$ and UIO-66, respectively. The reaction coordinates are denoted as structures I to VI in Fig. 10, where structure (I) is the representative isolated UIO-66$_{def}$. According to the free energy profile diagram, the stronger co-adsorption of vanillin and IPA on the UIO-66$_{def}$ represented in structure II assists the MPV process by the migration of hydride from the adsorbed IPA (Zr1) to the adsorbed vanillin (Zr2), resulting in the formation of structure III, where the vanillyl alcohol anion ((4-hydroxy-3-methoxyphenyl) methanolate) remain adsorbed on Zr2. Next, the IPA is again activated around the Zr1 sites, and the adsorbed vanillyl alcohol anion at Zr2 approaches this activated IPA (Structure IV), followed by the etherification reaction to form 4-(isopropoxymethyl)− 2-methoxyphenol (Structure V). The ether intermediate remained adsorbed at the Zr2 sites due to the cooperative involvement of the Zr Lewis acidity and μ$_3$ −O dynamic acidity, which further reacts with the adsorbed IPA at Zr1 sites to produce MMP as the final product (structure VI). A similar free energy profile diagram for UIO-66 mediated vanillin CTHDO using IPA is

presented in Fig. S13. It can be seen that the reaction coordinates are located at a higher free energy region than the UIO-66$_{def}$. Thus, the theoretical investigation further coincided with the experimental observation and suggested the superior reactivity of UIO-66$_{def}$ in the CTHDO of vanillin.

3.3. Proposed reaction mechanism and recycling test

Based on the experimental results and their validation through the DFT calculation as presented in the reaction coordinates free energy diagram, a reaction mechanism for the CTHDO of vanillin over UIO-66$_{def}$ is proposed (Scheme 3). In the first step of the reaction, the vanillin adsorbs on the unsaturated Zr Lewis site of UIO-66$_{def}$ (structure I), and the IPA adsorbs cum activated by the Zr−OH to form the complex structure II (Scheme 3). Subsequently, these active sites facilitate the hydrogen transfer from IPA to the C=O of vanillin by following the MPV pathway to form structure III. Due to the higher surface acidity, the vanillyl alcohol remains adsorbed on the UIO-66$_{def}$ (structure IV) and immediately participates in the etherification reaction with IPA (structure V). The C−O bond in the ether intermediate is polarized by its adsorption on the Zr Lewis acid sites and hence, participates in the hydrogenolysis reaction to form the MMP, as shown in structure VI in Scheme 3. It regenerates the catalyst system I to continue the CTHDO cycle. Similarly, the UIO-66 only afforded a low amount of ether intermediate due to the unavailability of the required active sites for the
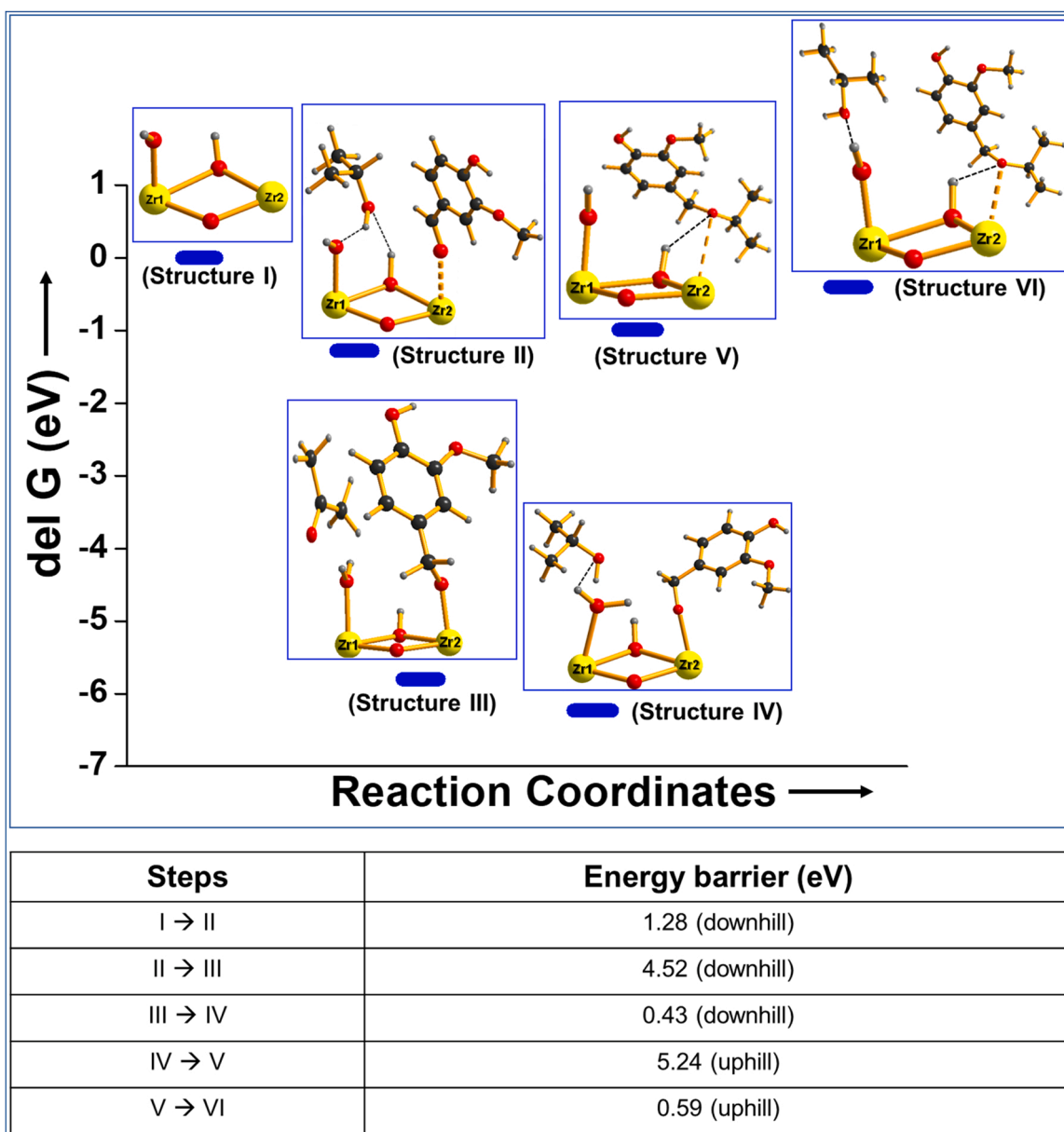
Steps	Energy barrier (eV)
I → II	1.28 (downhill)
II → III	4.52 (downhill)
III → IV	0.43 (downhill)
IV → V	5.24 (uphill)
V → VI	0.59 (uphill)

Fig. 10. Free energy diagram of the reaction coordinates for the reaction of vanillin and IPA over UIO-66$_{def}$ (The corresponding energy differences between the adjacent steps are presented in the table).
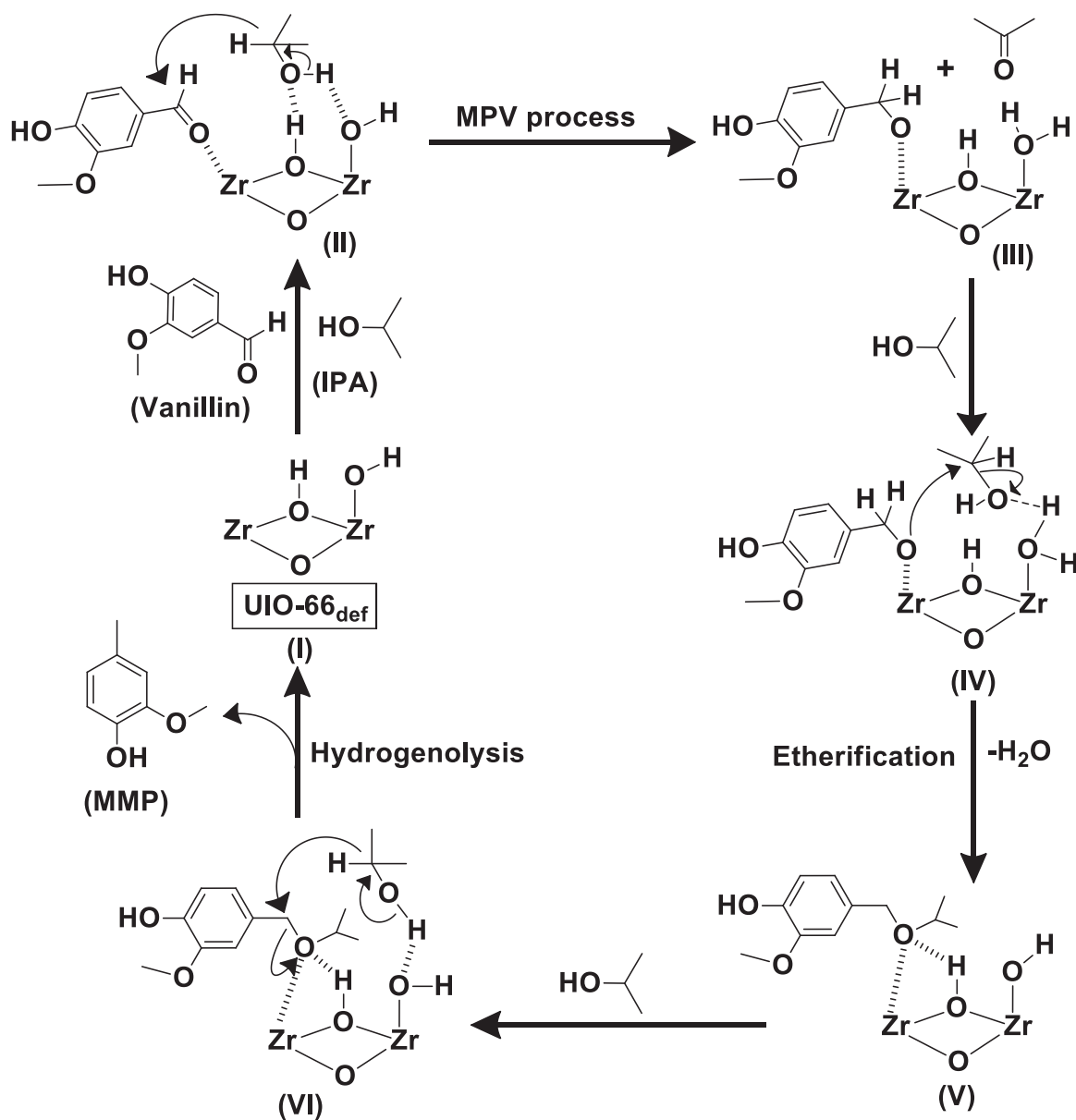
vanillin to MMP conversion. Based on the catalytic activity data and reaction coordinates vs. free energy diagram, a reaction mechanism corresponding to the vanillin conversion to the ether intermediate over UIO-66 is proposed (Scheme S1).

The stability and the reusability tests were conducted to ensure the UIO-66$_{def}$ is a robust heterogeneous catalyst for the vanillin CTHDO reaction. The recyclability experiment of UIO-66$_{def}$ was conducted at a lower MMP production (reaction time = 1 h) under the optimized condition. The recyclability experiment of UIO-66$_{def}$ in the CTHDO of vanillin was conducted for five consecutive cycles (Fig. S14a). After each cycle, UIO-66$_{def}$ was separated from the reaction mixture, washed with ethanol, and dried in an oven. It was treated further using Soxhlet extraction with DCM two times to remove the organic residuals and dried in a vacuum oven before using it in the next cycle. The recyclability study suggests only an acceptable loss in the catalytic activity after five cycles. The recycled catalyst was characterized by PXRD, BET, and HR-TEM analyses to ascertain its structural stability (Fig. S15, Table 1). The heterogeneity of the CTHDO of vanillin was also tested using the

hot-filtration test (leaching experiment). In the hot-filtration test, after 1 h of the CTHDO reaction, the catalyst was removed from the reaction mixture and continued the reaction without the UIO-66$_{def}$. It can be seen from Fig. S14b that the catalytic activity was seized after the catalyst was removed from the reaction mixture, which ruled out the homogeneous contribution of the catalyst in this reaction. Moreover, the reaction mixture was analyzed by the MP-AES analysis. No trace of Zr species was found in the reaction mixture, confirming the stability of UIO-66$_{def}$ and the heterogeneity of the vanillin CTHDO reaction.

4. Conclusions

In conclusion, the defect-generated UIO-66 MOF, i.e., UIO-66$_{def}$ was synthesized and extensively investigated to determine the mechanistic pathway for the CTHDO of vanillin using 2-propanol as the hydrogen source. The defect was quantified using TGA, and established by ^{1}H NMR. The high catalytic activity of UIO-66$_{def}$ in the exclusive conversion of vanillin to MMP (vanillin conversion of ~100 % and MMP selectivity

Scheme 3. A proposed reaction mechanism of CTHDO of vanillin using UIO-66$_{def}$.

of ~100 %) arose due to the defect-induced modulated acidity in the framework after the defect creation. The required acidic environment for the MMP production under the vanillin CTHDO route was accomplished by the cluster-defect creation in the UIO-66 framework. Generation of the **reo** phase in UIO-66$_{def}$ (confirmed by PXRD), weakening of framework C═O bond (confirmed by FT-IR), and positive shifts in the binding energy of constituent's elements confirmed the missing linkers in UIO-66$_{def}$. The total acidity increased and modulated compared to the UIO-66 after the missing linker in the framework, confirmed by the NH$_3$-TPD analysis and CD$_3$CN drift FT-IR analysis. The FT-IR drift analysis for the desorption of CD$_3$CN and IPA with temperature demonstrated the evolution of framework acidity in UIO-66$_{def}$. Furthermore, the poisoning experiment using the pyridine and 2,6-lutidine confirmed the involvement of Lewis acidity and Bronsted acidity in the vanillin conversion and MMP production during CTHDO of vanillin. The uncoordinated Zr sites behave as the Lewis acid sites, which were responsible for the vanillin conversion to an ether intermediate that subsequently converted to the MMP via the dynamic Bronsted acidity of the UIO-66$_{def}$. Experimental results were validated by the periodic DFT calculation. The DFT analysis suggested that the vanillin conversion and MMP production were

facilitated by the high adsorption energy values during the co-adsorption of vanillin and IPA on the UIO-66$_{def}$ framework than UIO-66. The free energy diagram of the reaction coordinates involved in the vanillin CTHDO was stepwise optimized by the DFT calculation to depict the reaction mechanism involved in the CTHDO of vanillin using UIO-66$_{def}$. The UIO-66$_{def}$ was a true heterogeneous catalyst and was recycled for several catalytic cycles with negligible loss in catalytic activity. A cheap transition metal catalyst, a user-friendly sustainable catalytic process, and detailed mechanistic studies through DFT calculations are attractive features of this study.

CRediT authorship contribution statement

Ashish Kumar Kar: Conceptualization, all experimental work including majority of characterizations, manuscript draft preparation. **Arjun K. Manal:** A few catalytic experiments and catalyst characterization. **Ranjini Sarkar:** DFT calculation. **Ravi Kumar:** Resources person (DFT study). **Sudip Chakraborty:** Supervision, Writing – review & editing (DFT part). **Rajeev Ahuja:** Supervision (DFT), **Rajendra Srivastava:** Main project investigator, Conceptualization, Supervision,

Writing – review & editing.

Declaration of Competing Interest

The authors declare that they have no known competing financial interests or personal relationships that could have appeared to influence the work reported in this paper.

Data availability

Data will be made available on request.

Acknowledgements

Appendix A. Supporting information

Supplementary data associated with this article can be found in the online version at doi:10.1016/j.apcatb.2023.122385.

References

[1] C. Li, X. Zhao, A. Wang, G.W. Huber, T. Zhang, Catalytic transformation of lignin for the production of chemicals and fuels, Chem. Rev. 115 (2015) 11559–11624.
[2] Z. Zhang, J. Song, B. Han, Catalytic transformation of lignocellulose into chemicals and fuel products in ionic liquids, Chem. Rev. 117 (2017) 6834–6880.
[3] B. Tang, W. Li, X. Zhang, B. Zhang, H. Zhang, C. Li, Depolymerization of Kraft lignin to liquid fuels with MoS₂ derived oxygen-vacancy-enriched MoO₃ in a hydrogen-donor solvent system, Fuel 324 (2022), 124674.
[4] X. Zhang, W. Li, J. Wang, B. Zhang, G. Guo, C. Shen, Y. Jiang, Depolymerization of Kraft lignin into liquid fuels over a WO₃ modified acid-base coupled hydrogenation catalyst, Fuel 323 (2022), 124428.
[5] D.M. Alonso, S.H. Hakim, S. Zhou, W. Won, O. Hosseinaei, J. Tao, V. Garcia-Negron, A.H. Motagamwala, M.A. Mellmer, K. Huang, C.J. Houtman, N. Labbe, D. P. Harper, C. Maravelias, T. Runge, J.A. Dumesic, Increasing the revenue from lignocellulosic biomass: maximizing feedstock utilization, Sci. Adv. 3 (2017), e1603301.
[6] C.H. Zhou, X. Xia, C.X. Lin, D.S. Tong, J. Beltramini, Catalytic conversion of lignocellulosic biomass to fine chemicals and fuels, Chem. Soc. Rev. 40 (2011) 5588–5617.
[7] J. Zakzeski, P.C. Bruijnincx, A.L. Jongerius, B.M. Weckhuysen, The catalytic valorization of lignin for the production of renewable chemicals, Chem. Rev. 110 (2010) 3552–3599.
[8] R. Fan, C. Chen, M. Han, W. Gong, H. Zhang, Y. Zhang, H. Zhao, G. Wang, Highly dispersed copper nanoparticles supported on activated carbon as an efficient catalyst for selective reduction of vanillin, Small 14 (2018) 1801953.
[9] J. Gao, Y. Cao, G. Luo, J. Fan, J.H. Clark, S. Zhang, High-efficiency catalytic hydrodeoxygenation of lignin-derived vanillin with nickel-supported metal phosphate, Chem. Eng. J. 448 (2022), 137723.
[10] J.L. Santos, M. Alda-Onggar, V. Fedorov, M. Peurla, K. Eranen, P. Mäki-Arvela, M. A. Centeno, D.Y. Murzin, Hydrodeoxygenation of vanillin over carbon supported metal catalysts, Appl. Catal. A 561 (2018) 137–149.
[11] A.B. Bindwal, P.D. Vaidya, Reaction kinetics of vanillin hydrogenation in aqueous solutions using a Ru/C catalyst, Energy Fuels 28 (2014) 3357–3362.
[12] L. Petitjean, R. Gagne, E.S. Beach, D. Xiao, P.T. Anastas, Highly selective hydrogenation and hydrogenolysis using a copper doped porous metal oxide catalyst, Green Chem. 18 (2016) 150–156.
[13] A.P. Pinheiro Pires, J. Arauzo, I. Fonts, M.E. Domine, A. Fernandez Arroyo, M. E. Garcia-Perez, J. Montoya, F. Chejne, P. Pfromm, M. Garcia-Perez, Challenges and opportunities for bio-oil refining: a review, Energy Fuels 33 (2019) 4683–4720.
[14] D. Wang, D. Astruc, The golden age of transfer hydrogenation, Chem. Rev. 115 (2015) 6621–6686.
[15] M.J. Gilkey, B. Xu, Heterogeneous catalytic transfer hydrogenation as an effective pathway in biomass upgrading, ACS Catal. 6 (2016) 1420–1436.
[16] A.K. Kar, R. Srivastava, An efficient and sustainable catalytic reduction of carbon-carbon multiple bonds, aldehydes, and ketones using a Cu nanoparticle decorated metal-organic framework, New J. Chem. 42 (2018) 9557–9567.
[17] W. Fang, A. Riisager, Recent advances in heterogeneous catalytic transfer hydrogenation/hydrogenolysis for valorization of biomass-derived furanic compounds, Green Chem. 23 (2021) 670–688.
[18] A.K. Kar, R. Srivastava, Reductive formylation of nitroarenes using HCOOH over bimetallic C–N framework derived from the Integration of MOF and COF, ChemCatChem 13 (2021) 3174–3183.
[19] Arzoo Chauhan, A.K. Kar, R. Srivastava, Ru-decorated N-doped carbon nanoflakes for selective hydrogenation of levulinic acid to γ-valerolactone and quinoline to tetrahydroquinoline with HCOOH in water, Appl. Catal. A Gen. 636 (2022), 118580.
[20] A.K. Kar, R. Srivastava, Solvent-dependent, formic acid-mediated, selective reduction and reductive N-formylation of N-heterocyclic arenes with sustainable cobalt-embedded N-doped porous carbon catalyst, ACS Sustain. Chem. Eng. 7 (2019) 13136–13147.
[21] Z. An, J. Li, Recent advances in the catalytic transfer hydrogenation of furfural to furfuryl alcohol over heterogeneous catalysts, Green Chem. 24 (2022) 1780–1808.
[22] A.S. Nagpure, A.K. Venugopal, N. Lucas, M. Manikandan, R. Thirumalaiswamy, S. Chilukuri, Renewable fuels from biomass derived compounds: Ru containing hydrotalcites as catalysts for conversion of HMF to 2,5-dimethylfuran, Catal. Sci. Technol. 5 (2015) 1463–1472.
[23] A. Kumar, A.K. Kar, R. Bal, R. Srivastava, Unraveling the synergistic participation of Ni–Sn in nanostructured NiO/SnO₂ for the catalytic transfer hydrogenolysis of benzyl phenyl ether, Energy Fuels 36 (2022) 4404–4415.
[24] Z. Yu, F. Meng, Y. Wang, Z. Sun, Y. Liu, C. Shi, W. Wang, A. Wang, Catalytic transfer hydrogenation of levulinic acid to γ-valerolactone over Ni₃P-CePO₄ catalysts, Ind. Eng. Chem. Res. 59 (2020) 7416–7425.
[25] J. He, H. Li, A. Riisager, S. Yang, Catalytic transfer hydrogenation of furfural to furfuryl alcohol with recyclable Al–Zr@Fe mixed oxides, ChemCatChem 10 (2018) 430–438.
[26] M. Koehle, R.F. Lobo, Lewis acidic zeolite Beta catalyst for the Meerwein–Ponndorf–Verley reduction of furfural, Catal. Sci. Technol. 6 (2016) 3018–3026.
[27] A.K. Manal, J.H. Advani, R. Srivastava, Bifunctional acid-base zirconium phosphonate for catalytic transfer hydrogenation of levulinic acid and cascade transformation of furfural to biofuel molecules, ChemCatChem 14 (1–10) (2022), e202200576.
[28] P. Vasanthakumar, R. Karvembu, Unmodified maghemite from river sand as a selective catalyst for base-free transfer hydrogenation of furfural, levulinic acid, and o-vanillin: a pathway for sustainable biomass conversions, ACS Sustain. Chem. Eng. 8 (2020) 17069–17078.
[29] K. Zhou, J. Chen, Y. Cheng, Z. Chen, S. Kang, Z. Cai, Y. Xu, J. Wei, Enhanced catalytic transfer hydrogenation of biomass-based furfural into 2-methylfuran over multifunctional Cu–Re bimetallic catalysts, ACS Sustain. Chem. Eng. 8 (2020) 16624–16636.
[30] G. Li, H. Li, Enhancing activity of Ni₂P-based catalysts by a yolk–shell structure and transition metal-doping for catalytic transfer hydrogenation of vanillin, Energy Fuels 35 (2021) 4158–4168.
[31] Q. Liao, M. Shi, Q. Zhang, W. Cheng, P. Ji, X. Fu, H. Lai, R. Fan, J. Sheng, H. Li, Gold catalyst anchored to pre-reduced Co₃O₄ nanorods for the hydrodeoxygenation of vanillin using alcohols as hydrogen donors, ACS Appl. Mater. Interfaces 14 (2022) 3939–3948.
[32] Z. Gao, F. Liu, L. Wang, F. Luo, Highly efficient transfer hydrodeoxygenation of vanillin over Sn4+-induced highly dispersed Cu-based catalyst, Appl. Surf. Sci. 480 (2019) 548–556.
[33] R. Nie, X. Peng, H. Zhang, X. Yu, X. Lu, D. Zhou, Q. Xia, Transfer hydrogenation of bio-fuel with formic acid over biomass-derived N-doped carbon supported acid-resistant Pd Catalyst, Catal. Sci. Technol. 7 (2017) 627–634.
[34] P. Wu, D. Zhao, G. Lu, C. Cai, Supported Pd–Au bimetallic nanoparticles as an efficient catalyst for the hydrodeoxygenation of vanillin with formic acid at room temperature, Green Chem. 24 (2022) 1096–1102.
[35] C.A. Smith, F. Brandi, M. Al-Naji, R. Guterman, Resin-supported iridium complex for low-temperature vanillin hydrogenation using formic acid in water, RSC Adv. 11 (2021) 15835–15840.
[36] Q. Wang, D. Astruc, State of the art and prospects in metal–organic framework (MOF)-based and MOF-derived nanocatalysis, Chem. Rev. 120 (2020) 1438–1511.
[37] A. Corma, H. Garcia, F.X. Llabres i Xamena, Engineering metal organic frameworks for heterogeneous catalysis, Chem. Rev. 110 (2010) 4606–4655.
[38] A.K. Kar, S.P. Kaur, T.J.D. Kumar, R. Srivastava, Efficient hydrogenolysis of aryl ethers over Ce-MOF supported Pd NPs under mild conditions: mechanistic insight using density functional theoretical calculations, Catal. Sci. Technol. 10 (2020) 6892–6901.
[39] A.K. Kar, R. Srivastava, Improving the glucose to fructose isomerization via epitaxial-grafting of niobium in UIO-66 framework, ChemCatChem 14 (1–12) (2022), e202200721.
[40] C. Xu, Y. Pan, G. Wan, H. Liu, L. Wang, H. Zhou, S.H. Yu, H.L. Jiang, Turning on visible-light photocatalytic C–H oxidation over metal–organic frameworks by introducing metal to-cluster charge transfer, J. Am. Chem. Soc. 141 (2019) 19110–19117.
[41] J.M. Guarinos, F.G. Cirujano, A. Rapeyko, F.X.L. Xamena, Conversion of levulinic acid to γ-valerolactone over Zr-containing metal-organic frameworks: evidencing the role of Lewis and Brønsted acid sites, Mol. Catal. 515 (2021), 111925.
[42] F. Wang, Z. Chen, H. Chen, T.A. Goetjen, P. Li, X. Wang, S. Alayoglu, K. Ma, Y. Chen, T. Wang, T.N. Islamoglu, Y. Fang, R.Q. Snurr, O.K. Farha, Interplay of lewis and Brønsted acid sites in Zr-based metal–organic frameworks for efficient esterification of biomass-derived levulinic acid, ACS Appl. Mater. Interfaces 11 (2019) 32090–32096.

[43] C. Ye, Z. Qi, D. Cai, T. Qiu, Design and synthesis of ionic liquid supported hierarchically porous Zr metal−organic framework as a novel Brønsted−Lewis acidic catalyst in biodiesel synthesis, Ind. Eng. Chem. Res. 58 (2019) 1123–1132.

[44] M. Qiu, T. Guo, R. Xi, D. Li, X. Qi, highly efficient catalytic transfer hydrogenation of biomass-derived furfural to furfuryl alcohol using UiO-66 without metal catalysts, Appl. Catal. A Gen. 602 (1−7) (2020), 117719.

[45] A.H. Valekar, M. Lee, J.W. Yoon, J. Kwak, D.Y. Hong, K.R. Oh, G.Y. Cha, Y. U. Kwon, J. Jung, J.S. Chang, Y.K. Hwang, Catalytic transfer hydrogenation of furfural to furfuryl alcohol under mild conditions over Zr-MOFs: exploring the role of metal node coordination and modification, ACS Catal. 10 (2020) 3720–3732.

[46] L. Valenzano, B. Civalleri, S. Chavan, S. Bordiga, M.H. Nilsen, S. Jakobsen, K. P. Lillerud, C. Lamberti, Disclosing the complex structure of UiO-66 metal organic framework: a synergic combination of experiment and theory, Chem. Mater. 23 (2011) 1700–1718.

[47] J. Sittiwong, S. Boonmark, W. Nunthakitgoson, T. Maihom, C. Wattanakit, J. Limtrakul, Density functional investigation of the conversion of furfural to furfuryl alcohol by reaction with i-propanol over UiO-66 metal–organic framework, Inorg. Chem. 60 (2021) 4860–4868.

[48] F.G. Cirujano, F.X. Llabres i Xamena, Tuning the catalytic properties of UiO-66 metal-organic frameworks: from Lewis to defect-induced Brønsted acidity, J. Phys. Chem. Lett. 11 (2020) 4879–4890.

[49] C.A. Trickett, K.J. Gagnon, S. Lee, F. Gándara, H.B. Bürgi, O.M. Yaghi, Definitive molecular level characterization of defects in UiO-66 crystals, Angew. Chem. Int. Ed. 54 (2015) 11162–11167.

[50] G.C. Shearer, S. Chavan, S. Bordiga, S. Svelle, U. Olsbye, K.P. Lillerud, Defect engineering: tuning the porosity and composition of the metal-organic framework UiO-66 via modulated synthesis, Chem. Mater. 28 (2016) 3749–3761.

[51] Y. Feng, Q. Chen, M. Jiang, J. Yao, Tailoring the properties of UiO-66 through defect engineering: a review, Ind. Eng. Chem. Res. 58 (2019) 17646–17659.

[52] J. Jiang, W. Ding, W. Zhang, H. Li, Defect-rich ZrO₂ anchored Pd nanoparticles for selective hydrodeoxygenation of bio-models at room temperature, Fuel 318 (1−8) (2022), 123529.

[53] D. de la Flor, C. López-Aguado, M. Paniagua, G. Morales, R. Mariscal, J.A. Melero, Defective UiO-66 (Zr) as an efficient catalyst for the synthesis of bio jet-fuel precursors via aldol condensation of furfural and MIBK, J. Catal. 401 (2021) 27–39.

[54] O. Karagiaridi, W. Bury, J.E. Mondloch, J.T. Hupp, O.K. Farha, Solvent-assisted linker exchange: an alternative to the de novo synthesis of unattainable metal–organic frameworks, Angew. Chem. Int. Ed. 53 (2014) 4530–4540.

[55] X. Zhang, Y. Yang, L. Song, J. Chen, Y. Yang, Y. Wang, Enhanced adsorption performance of gaseous toluene on defective UiO-66 metal organic framework: equilibrium and kinetic studies, J. Hazard. Mater. 365 (2019) 597–605.

[56] X. Feng, J. Hajek, H.S. Jena, G. Wang, S.K.P. Veerapandian, R. Morent, N. De Geyter, K. Leyssens, A.E.J. Hoffman, V. Meynen, C. Marquez, D.E. De Vos, V. Van Speybroeck, K. Leus, P. Van Der Voort, Engineering a highly defective stable UiO-66 with tunable Lewis- Bronsted acidity: The role of the hemilabile linker, J. Am. Chem. Soc. 142 (2020) 3174–3183.

[57] X. Zhang, X. Shi, J. Chen, Y. Yang, G. Lu, The preparation of defective UiO-66 metal-organic framework using MOF-5 as structural modifier with high sorption capacity for gaseous toluene, J. Environ. Chem. Eng. 7 (1−8) (2019), 103405.

[58] X. Shi, X. Zhang, F. Bi, Z. Zheng, L. Sheng, J. Xu, Z. Wang, Y. Yang, Effective toluene adsorption over defective NH₂-UiO-66: an experimental and computational exploration, J. Mol. Liq. 316 (1−13) (2020), 113812.

[59] S. Subhan, M. Yaseen, B. Ahmad, Z. Tong, F. Subhan, W. Ahmad, M. Sahibzada, Fabrication of MnO₂ NPs incorporated UiO-66 for the green and efficient oxidative desulfurization and denitrogenation of fuel oils, J. Environ. Chem. Eng. 9 (1−15) (2021), 105179.

[60] R. Wei, C.A. Gaggioli, G. Li, T. Islamoglu, Z. Zhang, P. Yu, O.K. Farha, C.J. Cramer, L. Cagliardi, D. Yang, Tuning the properties of Zr₆O₈ nodes in the metal organic framework UiO-66 by selection of node-bound ligands and linkers, Chem. Mater. 31 (2019) 1655–1663.

[61] J. Liang, R.P. Chen, X.Y. Wang, T.T. Liu, X.S. Wang, Y.B. Huang, R. Cao, Postsynthetic ionization of an imidazole-containing metal-organic framework for the cycloaddition of carbon dioxide and epoxides, Chem. Sci. 8 (2017) 1570–1575.

[62] A.H. Valekar, K.-H. Cho, S.K. Chitale, D.-Y. Hong, G.-Y. Cha, U.-H. Lee, D. Hwang, C. Serre, J.S. Chang, Y.-K. Hwang, Catalytic transfer hydrogenation of ethyl levulinate to γ-valerolactone over zirconium-based metal-organic frameworks, Green Chem. 18 (2016) 4542–4552.

[63] S. Rojas-Buzo, B. Bohigues, C.W. Lopes, D.M. Meira, M. Boronat, M. Moliner, A. Corma, Tailoring Lewis/Brønsted acid properties of MOF nodes via hydrothermal and solvothermal synthesis: simple approach with exceptional catalytic Implications, Chem. Sci. 12 (2021) 10106–10115.

[64] B.S. Rao, D.D. Lakshmi, P.K. Kumari, N. Lingaiah, Influence of metal oxide and heteropoly tungstate location in mesoporous silica towards catalytic transfer hydrogenation of furfural to γ-valerolactone, Sustain. Energy Fuels 5 (2021) 3719–3728.

[65] B. Saini, A.P. Tathod, J. Diwakar, S. Arumugam, N. Viswanadham, Nickel nano-particles confined in ZSM-5 framework as an efficient catalyst for selective hydrodeoxygenation of lignin-derived monomers, Biomass Bioenergy 157 (1−10) (2022), 106350.

[66] N. Chen, N. Wang, Y. Ren, H. Tominaga, E.W. Qian, Effect of surface modification with silica on the structure and activity of Pt/ZSM-22@SiO₂ catalysts in hydrodeoxygenation of methyl palmitate, J. Catal. 345 (2017) 124–134.

[67] R.S. Mulliken, Electronic Population Analysis on LCAO-MO Molecular wave functions. IV. Bonding and antibonding in LCAO and valence-bond theories, J. Chem. Phys. 23 (1−4) (1955) 2343.

[68] R. Sarkar, T.K. Kundu, Density functional theory-based analyses on selective gas separation by β-PVDF-supported ionic liquid membranes, J. Mol. Graph. Model. 108 (1−34) (2021) 108004.